



Efficient and stable core-shell α -Fe₂O₃/WS₂/WO_x photoanode for oxygen evolution reaction to enhance photoelectrochemical water splitting

Zohreh Masoumi^{a,1}, Meysam Tayebi^{b,1}, Morteza Kolaei^a, Byeong-Kyu Lee^{a,*}

^a Department of Civil and Environment Engineering, University of Ulsan, Daehakro 93, Namgu, Ulsan 44610, Republic of Korea

^b Advanced Industrial Chemistry Research Center, Advanced Convergent Chemistry Division, Korea Research Institute of Chemical Technology (KRICT), 45 Jonggaro, Ulsan 44412, Republic of Korea

ARTICLE INFO

Keywords:

Photoelectrochemical (PEC) water splitting
 α -Fe₂O₃ nanorod
 Exfoliated WS₂ nanosheets
 Core-shell structured
 Heterojunction

ABSTRACT

In the present work, the WS₂ nanosheets were prepared through a liquid-phase exfoliation method (LPE). Various techniques were then used to characterize thickness, length, and concentration of these nanosheets. WS₂ nanosheets were also loaded on α -Fe₂O₃ photoanodes to prepare core-shell structured α -Fe₂O₃/WS₂/WO_x photoanodes. These core-shell structured α -Fe₂O₃/WS₂/WO_x nanorods have advantages of effective separation, decreased recombination of photo-generated electron-hole pairs, and increased electron transport properties, resulting in improved PEC performance. The best photoanode (α -Fe₂O₃/4-WS₂/WO_x) had photocurrent densities of 0.98 and 2.1 mA cm⁻² (with the lowest onset potential 0.54 V_{RHE} and 0.47 V_{RHE}) under front and back-side illumination, respectively, at 1.23 V_{RHE} under 100 mW cm⁻², which were about 13 and 30-fold higher than those of pure α -Fe₂O₃ photoelectrode. Furthermore, H₂ and O₂ production of α -Fe₂O₃/4-WS₂/WO_x photoanode were 32 μ mol.cm⁻² and 15.3 μ mol.cm⁻², respectively at 1.23 V_{RHE} under 100 mW cm⁻² after 2 h.

1. Introduction

Photoelectrochemical (PEC) water splitting is one of the direct methods to convert solar energy into chemical energy which can then be converted into electricity. In the future, PEC water splitting will play a remarkable role in sustainable energy production for conquering environmental problems [1]. Although a considerable amount of research has already been performed in this area, proceed still requires to be made towards a high-efficiency water-splitting cell for solar-to-hydrogen fuel conversion [2]. Higher efficiency photoanodes are required for large-scale electricity generation. Different n-type semiconductors, such as TiO₂ [3], BiVO₄ [4], ZnO [5], and α -Fe₂O₃ [6] have been applied as photoanode materials to improve PEC performance [7,8].

Among them, hematite (α -Fe₂O₃) has received wide attention as an n-type semiconductor due to its suitable bandgap (2.1 eV), eco-friendliness, abundance, and high absorption range of ca. 40% solar radiation [9]. It has been reported that α -Fe₂O₃ has a maximum solar-to-hydrogen efficiency (15.3%) corresponding to a photocurrent density of ca. 12.6 mA.cm⁻² at 1.23 V versus a reversible hydrogen electrode (RHE) under 100 mW.cm⁻² illumination [10]. However,

α -Fe₂O₃ also has drawbacks such as significant charge recombination and short hole diffusion length ($L_D \approx 2$ –4 nm) [11]. Therefore, research studies investigating new and efficient methods to enhance PEC performance are still needed. One of the most effective strategies to overcome charge recombination is fabricating an appropriate heterojunction onto semiconductor surfaces [12].

At present, two-dimensional materials have exclusive potential and properties for various applications. Among two-dimensional materials, transition metal dichalcogenides (TMDs) have attracted attention due to their proper band position with (5–10) % light absorption in the visible range [13]. TMDs, especially MoS₂ and WS₂, have high catalytic activities with excellent stability for energy applications. This might because they have various active sites such as active metal sites (W or Mo) and covalent (S or Se) sites [14]. Exfoliated layers of WS₂ have unique properties such as high thermal and chemical stabilities, low coefficient of resistance, and proper band edge for enhanced visible light absorption [15]. Electronic properties of two-dimensional TMD materials are found to be strongly reliant on their morphology and preparation method. Exfoliated WS₂ in its bulk form has an indirect bandgap (1.35 eV). In a mono- or few-layered form, it becomes a direct band semiconductor (2.05 eV) with extraordinary optoelectronic properties [16]. Few layers

* Corresponding author.

E-mail address: bklee@ulsan.ac.kr (B.-K. Lee).

¹ Equal contributions.

of WS₂ nanosheets have a S-W-S structure as a graphene-like layer construction consisting of two close-packed sulfur atom layers and one tungsten atom layer. These layers are feebly kept together by van der Waals forces, presenting a large active surface with broad light absorption. In contrast with layered MoS₂, WS₂ has a higher electrical conductivity. Thus, it is preferable for the fabrication of hybrid composites to elevate the PEC of HER/OER systems by integrating α -Fe₂O₃ nanomaterials. Moreover, a monolayer WS₂ nanosheet can be obtained with a direct liquid exfoliation method with a yield as high as 36%, depending on the type of solvent used [17].

Micro- and nano-scale core-shell structures have attracted great interest due to their unique properties in that their performances can be conveniently controlled by improving chemical compositions and morphologies of both core and shell. The overall performance of a core-shell system, even beneficial synergistic effects, can be adjusted by interactions between various ingredients of the core and shell. Most photocatalysts with a core-shell structure have TiO₂ based materials known to be active in the UV range. There are few visible light active core-shell structured materials due to the lack of effective synthetic methods [18]. Thus, developing high-performance visible light active photocatalysts with high visible light absorption efficiency, efficient charge separation properties, large surface area, and good stability and durability is important for the field of photocatalysis.

A few studies have reported the PEC performance of α -Fe₂O₃ modified with MoS₂ and other 2D materials. To the best of our knowledge, this is the first study investigating the PEC performance of WS₂ as a shell (which an amount of WS₂ was initially transformed to WO₄, WO₃, WO₂, WO⁺, WS⁺, WS₂⁺, S⁻ and W⁺ ions) fabricated by heterojunction with α -Fe₂O₃ nanorods.

The present work reports the fabrication of two dimensional WS₂ nanosheets with a few layers prepared by a liquid-phase exfoliation procedure in a solvent mixture (ethanol/water). They show advantages such as low toxicity, freedom from additives, and biocompatibility. These WS₂ nanosheets can be easily deposited onto α -Fe₂O₃ electrode surface by a facile and affordable process to fabricate a core-shell nanorod structure. In addition, core-shell WS₂ fabricated by heterojunction on α -Fe₂O₃ photoanode with the formation of WO_x (WO₄, WO₃, WO₂, and WO⁺ ions) on the top surface as a protection layer was confirmed using time of flight-secondary ion mass spectrometry (TOF-SIMS) analysis. More intriguingly, we prepared α -Fe₂O₃/#4-WS₂ (heat treatment at 90° C) and α -Fe₂O₃/#4-WS₂/WO_x (heat treatment at 450° C) electrodes to further explore the effect of heat treatment on the prepared shell, which is led to finding out the highest PEC water oxidation activity of α -Fe₂O₃/#4-WS₂/WO_x photoanode exhibits a strong dependence on the anions, which accelerates the movement of photogenerated charge carriers, thus boosting the OER activity. In addition, core-shell WS₂ fabricated by heterojunction on α -Fe₂O₃ photoanode with formation of WO_x (WO₄, WO₃, WO₂, and WO⁺ ions) on the top surface as a thin layer was confirmed using time of flight-secondary ion mass spectrometry (TOF-SIMS) analysis. Donor concentration (N_D), charge transfer resistance (R_{ct}), and average decay time (τ_{ave}) values were systematically estimated by Mott-Schottky, Electrochemical impedance spectroscopy (EIS), and Time-Resolved Photoluminescence (TRPL) analyses. These core-shell structured α -Fe₂O₃/#4-WS₂/WO_x photoanode have advantages of effective separation, decreased recombination of photo generated electron-hole pairs, and increased electron transport properties, resulting in improved PEC performance.

2. Experimental section

2.1. α -Fe₂O₃/#4-WS₂/WO_x photoelectrode preparation

2.1.1. α -Fe₂O₃ nanorods in thin film

Hematite (α -Fe₂O₃) precursors were synthesized by mixing 0.15 M FeCl₃·6H₂O and 1 M NaNO₃. HCl was then dropwise added to the mixture to adjust the pH of the mixture to 1.5. A cleaned FTO (Fluorine-

doped Tin Oxide) glass was placed at the bottom of a Teflon container. Then 80 mL of the solution was added into the Teflon container. The autoclave was set at 100 °C for 6 h. Surfaces of prepared β -FeOOH samples were then washed off with deionized water. Finally, the electrode was placed at 550 °C in a furnace in the air for 4 h to prepare α -Fe₂O₃ nanorods.

2.1.2. 2D-WS₂ nanosheets precursor

Exfoliated WS₂ nanosheets precursor was prepared with a liquid phase exfoliation (LPE) method. WS₂ bulk powder (300 mg) was dissolved in a mixture of ethanol (35 mL) with water (55 mL). The precursor was ultrasonicated continuously for five days. To separate WS₂ nanosheets, dispersions were centrifuged at 3500 rpm for 60 min. Afterwards, the supernatant including thin WS₂ nanosheets was collected from the top of the solution.

2.1.3. Core-shell α -Fe₂O₃/#n-WS₂/WO_x nanostructure

The core-shell structure of α -Fe₂O₃ and WS₂ was fabricated by a convenient and low-cost drop casting procedure. The WS₂ nanosheets precursor (100 μ L) was dropped onto the top surface of α -Fe₂O₃ electrode and put in a furnace at 350 °C for 5 min. The dropping process was repeated under similar circumstances for two, four, and eight times, which were labeled as α -Fe₂O₃/#2-WS₂/WO_x, α -Fe₂O₃/#4-WS₂/WO_x, and α -Fe₂O₃/#8-WS₂/WO_x, respectively. Finally, all prepared photoelectrodes were put in a furnace at 450 °C for 2 h. Fig. S1 at supporting information illustrates the synthesis process of the pure α -Fe₂O₃, α -Fe₂O₃/#n-WS₂, and α -Fe₂O₃/#n-WS₂/WO_x (n = 2,4,and 8) photoanodes.

2.2. Photoelectrochemical (PEC) measurement

A standard three-electrode cell was used for measuring the PEC performance. A platinum wire was used as a counter electrode. The α -Fe₂O₃, α -Fe₂O₃/#2-WS₂/WO_x, α -Fe₂O₃/#4-WS₂/WO_x, and α -Fe₂O₃/#8-WS₂/WO_x photoanodes were applied as working electrodes. Ag/AgCl was used as a reference electrode in 1 M NaOH (pH~14) electrolyte which was converted to RHE with Eq. 1:

$$V_{RHE} = V_{Ag/AgCl} + 0.197 + 0.059 \times \text{pH} \quad (1)$$

The PEC performance was measured under an illumination of 100 mW/cm² from a 300 W Xe lamp on the front- and back-side of photoelectrodes at a voltage range of 0.3–1.5 V_{RHE}. EIS was measured under different potential (0.9, 1, 1.1 V_{RHE}) with the identical electrode formation.

3. Results and discussion

3.1. Structural characterization for prepared WS₂

Atomic force microscopy (AFM) and near-infrared (NIR) to ultraviolet (UV) region were used to estimate the concentration, length, and thicknesses of exfoliated WS₂ nanosheets. Optical absorption of nanosheets were observed at three main exciton peaks A (~631 nm), B (~522 nm), and C (~423 nm) corresponding to its electronic band structure, indicating the existence of exfoliated WS₂ nanosheets (Fig. 1a). A and B exciton peaks were shifted by an accumulation of layers under ultrasonication time and centrifuge speed. The energy variation between peaks A and B was also increased by enhancing the layer's accumulation [19]. The C peak was attributed to van der Waals interactions. It is related to monolayered or multilayered materials. Values shown in peaks A, B, and C represented considerable contribution of few-layered nanosheets [20]. Raman analysis for WS₂ nanosheets showed strong signals at around 355 and 425 (cm⁻¹) corresponding to in-plane E_{2g} vibration and out-of-plane A_{1g} vibration, respectively (Fig. 1b). These two peaks were consistent with observed peaks of

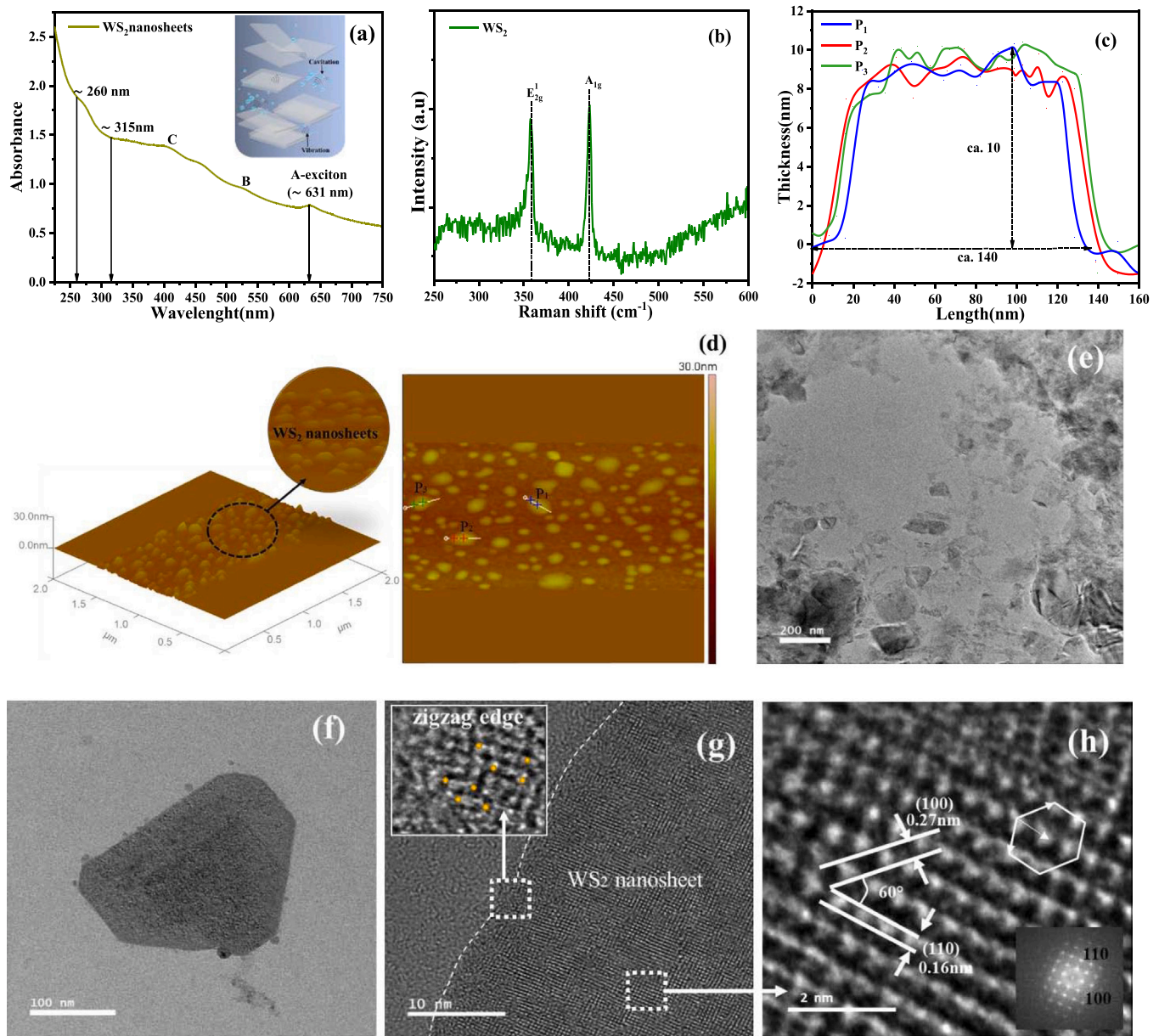


Fig. 1. a) UV-vis absorption spectrum (inside is schematic of ultrasonication effect in liquid-phase exfoliation method), b) Raman scattering excitation spectra, c and d) AFM image and height profile. e, f, and g) HR-TEM images for selected regions, inset of g) is hexagonal arrangement of atoms with inset image of the zigzag edges, and the inset of h) is the fast Fourier transform (FFT) pattern of the exfoliated WS₂ nanosheets.

exfoliated WS₂ nanosheets. As shown in Fig. 1c and d, AFM results indicated three points (P₁, P₂, and P₃). The highest profile diagram of these three exfoliated WS₂ nanosheets had thickness and length ca. 10 and 140 nm, respectively. For more investigation of experimental results, the length, thickness, and concentration of exfoliated WS₂ nanosheets were estimated by equations. To calculate thicknesses of WS₂ nanosheets, Eq. (2) [21] was used:

$$\text{Thickness(N(nm))} = 6.35 \times 10^{-32} \times \exp(\lambda_A/8.51) \quad (2)$$

In this equation, λ_A was the wavelength at peak A shown in Fig. 1a. The average thickness of few-layer WS₂ nanosheets in the prepared precursor was estimated to be approximately 10 nm, which revealed exfoliated multi-layers. This result was in good agreement with AFM results. The length (~140 nm) and concentration (~0.04 mg.mL⁻¹) of WS₂ nanosheets were calculated by Eq. (3) and (4), respectively [21]:

$$L(\text{nm}) = \frac{(2.3 - \frac{EXT_{235}}{EXT_{290}})}{(\frac{0.02EXT_{235}}{EXT_{290}} - 0.0185)} \quad (3)$$

$$C(\frac{\text{mg}}{\text{ml}}) = \frac{\text{Absorbance}(265\text{nm})}{\epsilon_{235\text{nm}}} \quad (4)$$

In Eq. (3), L was the average size of nanosheets, which was estimated by EXT₂₃₅ and EXT₂₉₀ values in UV-Vis data. The concentration of nanosheets in Eq. (4) depends on the absorbance value at wavelength 265 nm and the extinction coefficient at 235 nm, which is an invariant ($\epsilon_{235\text{nm}} = 47.7 \text{ L g}^{-1} \text{ cm}^{-1}$). Furthermore, the amount of WS₂ precursor per area of photoanode was estimated with Eq. (5) [15,21]:

$$\text{Amount of WS}_2\text{nanosheets per area} = \frac{\text{Times of drop} \times 100 \mu\text{L} \times C}{\text{photoelectrode's area}} \quad (5)$$

The schematic figure inside of Fig. 1a shows the application of

continuous ultrasonic waves or vibrations in aqueous surfactant solutions or organic solvents, which can be utilized to prevent changes in the electronic and chemical behavior of the WS₂ in the conversion process of bulk to nanosheets. Ultrasonic waves in the LPE method can make small bubbles or cavities in the solvent.

In the ultrasonication process, cavities are continuously imploding and emitting a burst of energy. This energy caused by the stationary wave pattern when passing through the organic solvent molecules in the cavities can maintain the WS₂ nanosheets, which in turn can prevent reaggregation. Therefore, the interface reaction among molecules of the solvent and WS₂ nanosheets is greater than interlayer forces joining the WS₂ sheets at the bulk crystal [22,23]. Furthermore, the thickness and uniformity of the deposited film were determined by AFM analysis of the WS₂ nanosheets precursor dropped on the clean surface two, four, and eight times (Fig. S2). The evidence showed that uniform WS₂ nanosheets on the surface could be stabilized during two and four times of drop-casting. However, the thickness of WS₂ at some parts of eight-time drop-casting was more than 10 nm, disturbing the uniformity of the surface. This agglomeration could be the reason for decreased PEC performance in α -Fe₂O₃/#8-WS₂/WO_x photoanode [24].

Further, the lattice structure of WS₂ nanosheets was investigated in high-resolution TEM (HRTEM) images (Fig. 1e–h) and two-dimensional fast Fourier transform (FFT) analysis (inside Fig. 1h). Fig. 1e shows the

prepared WS₂ nanosheet structure using a continuous ultrasonication process in the LPE method. Fig. 1f clearly confirms the existence of the two-dimensional morphology of WS₂ of (100–200) nm length. Fig. 1g demonstrates that the hexagonal structure of the WS₂ nanosheets is preserved during the sonication process. The top view of the hexagonal honeycomb geometry of the prepared WS₂ nanosheets with both zigzag edges, which is well-known for the high catalytic activity and electronic preferences for WS₂ nanosheets (Fig. 1g) [25]. The FFT image and electron diffraction pattern of the inner parts of one nanosheet (Fig. 1h), clearly show the hexagonal formation with two close lattice distances of (0.27 and 0.16) nm, which are in good accordance with the standard interplanar distances of the (100) and (110) planes of WS₂, respectively [26,27]. The TEM images of the prepared WS₂ nanosheets can also be attributed to homogenous tungsten and sulfur elements distribution in the whole individual WS₂ nanosheet.

3.2. Characterization for prepared α -Fe₂O₃/#n-WS₂/WO_x photoanodes

Morphologies of α -Fe₂O₃ and α -Fe₂O₃/#4-WS₂/WO_x structures were observed by SEM analysis (Fig. 2a–d). As shown in Fig. 2a and c, the SEM of the prepared α -Fe₂O₃ revealed rice-shaped nanorods with a random size vertically aligned on the FTO substrate. The morphology of the α -Fe₂O₃/#4-WS₂/WO_x nanorods became longer, denser, and wider

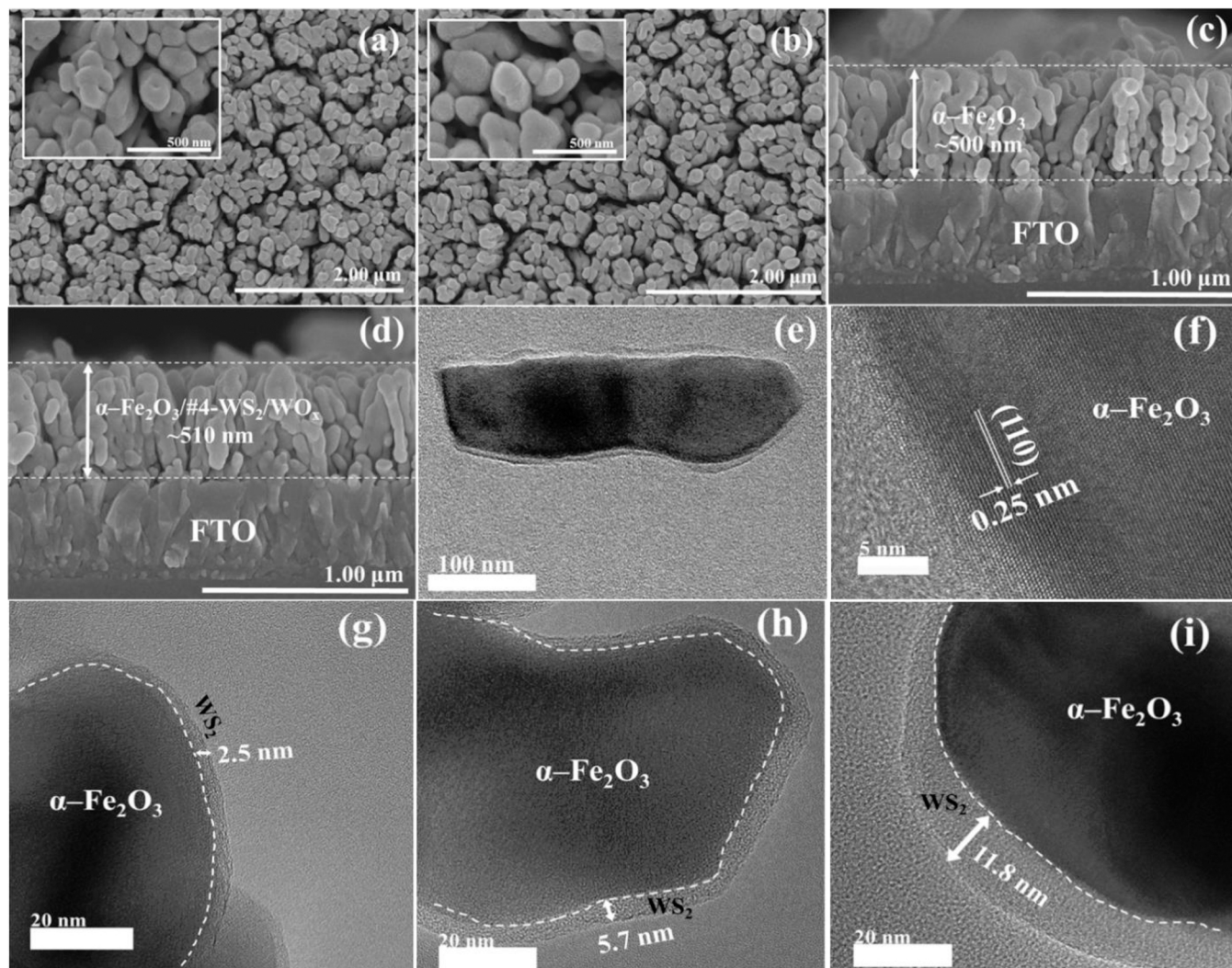


Fig. 2. Top-view FE-SEM images of a) pure α -Fe₂O₃ and b) α -Fe₂O₃/#4-WS₂/WO_x. Cross section images of c) pure α -Fe₂O₃ and d) α -Fe₂O₃/#4-WS₂/WO_x. e) HRTEM images of α -Fe₂O₃/#4-WS₂/WO_x core-shell nanorod structure, g) α -Fe₂O₃/#2-WS₂/WO_x, h) α -Fe₂O₃/#4-WS₂/WO_x, and i) α -Fe₂O₃/#8-WS₂/WO_x photoanodes.

after they were fabricated into heterojunction (Fig. 2b and d). The thickness of the α -Fe₂O₃/#4-WS₂/WO_x thin film increased very less. The SEM cross-section view of the α -Fe₂O₃/#4-WS₂/WO_x electrode is shown in Fig. 2c. Elemental mapping and energy dispersive X-Ray (EDX) analysis are shown in Fig. S3, confirming the existence of Fe, O, W, and S elements on the surface of photoelectrode.

Fig. 2(e–i) show high-resolution TEM images of the bare α -Fe₂O₃ and core-shell α -Fe₂O₃/#4-WS₂/WO_x photoanodes. HRTEM image in Fig. 2e clearly showed that the WS₂ completely surrounded α -Fe₂O₃ nanorod and made a core-shell structure. The identified lattice spacing for α -Fe₂O₃ nanorods was ~ 0.25 nm, which was relevant to the lattice plane (110) (Fig. 3f) [28,29]. The thickness of the WS₂ layers on the α -Fe₂O₃ nanorods was increased by repeating the drop-casting procedure from two to eight times, respectively, denoted as α -Fe₂O₃/#2-WS₂/WO_x, α -Fe₂O₃/#4-WS₂/WO_x, and α -Fe₂O₃/#8-WS₂/WO_x (Table 1). The thickness created by the exfoliated WS₂ nanosheets concentration on the surface of the α -Fe₂O₃ nanorods affected light-harvesting and charge separation of PEC performance. Moreover, dropping more WS₂ nanosheets precursor on the outer surface of the α -Fe₂O₃ nanorods directly affected the increase in the thickness of the shell. Therefore, high-resolution TEM images of α -Fe₂O₃/#2-WS₂/WO_x (Fig. 2g), α -Fe₂O₃/#4-WS₂/WO_x (Fig. 2h), and α -Fe₂O₃/#8-WS₂/WO_x (Fig. 2i) showed different thickness of WS₂ nanosheets on the α -Fe₂O₃ nanorods of around 2.5, 5.7, and 11.8 nm, respectively. It may be noted that tungsten oxide is thermodynamically more stable than tungsten disulfide even at room temperature. Therefore, the uniformity of the thickness for WS₂ nanosheets after the heat treatment process on the α -Fe₂O₃ nanorods and the oxidation reaction depend on various parameters such as the concentration of oxygen, time, temperature, and defect chemistry of the material. Moreover, the

formation of WO_x (WO₃, WO₂, and WO[•] ions) on the top surface with a lower distance between neighboring W atoms or a smaller size in the case of W⁺ ion might make the thickness of the shell (prepared after dropping two, four, and eight times WS₂ and heat treatment) to be less than that of the pure WS₂ nanosheets in the precursor. Finally, the optimum state with four times repeated droppings of WS₂ nanosheets precursor on the α -Fe₂O₃ electrode (α -Fe₂O₃/#4-WS₂/WO_x) fabricated shells with a proper thickness of around 5.7 nm, which was found to have the best PEC performance. Therefore, the α -Fe₂O₃/#4-WS₂/WO_x photoelectrode with a well-prepared core-shell structure for efficient light-harvesting can improve the charge separation, causing the best PEC performance.

Fig. 3a shows results of high-resolution X-ray diffraction (HRXRD) analysis of pure α -Fe₂O₃, α -Fe₂O₃/#4-WS₂, and α -Fe₂O₃/#4-WS₂/WO_x electrodes. Peaks at the prepared samples all exhibit similar XRD patterns of the α -Fe₂O₃ phase (JCPDS-33-0664). This information indicates that the crystallographic structure of hematite in the α -Fe₂O₃/#4-WS₂ and α -Fe₂O₃/#4-WS₂/WO_x electrodes are the same as that in the pure α -Fe₂O₃ sample [30]. Diffraction peaks at around 14.6° correspond to the (002) planes can be related to the hexagonal WS₂ structure at α -Fe₂O₃/#4-WS₂ and α -Fe₂O₃/#4-WS₂/WO_x electrodes (JCPDF No. 08-0237) [31]. Furthermore, the diffraction peaks at 2 θ of around 23.5° correspond to the (002) facets for WO₃ nanostructure [32].

Raman spectra of pure α -Fe₂O₃, α -Fe₂O₃/#4-WS₂ and α -Fe₂O₃/#4-WS₂/WO_x photoanodes are shown in Fig. 3b. Peaks were observed at 228.2, 293.6, 409.9, 499.8, 609.6, and 1315.4 cm⁻¹, confirming Raman active modes of α -Fe₂O₃ [33]. The Raman spectra of WS₂ were observed at ~ 350 cm⁻¹ for the E_{2g} and at ~ 420 cm⁻¹ for the A_g¹ at the α -Fe₂O₃/#4-WS₂ and α -Fe₂O₃/#4-WS₂/WO_x (Fig. 3b) [34]. When the WS₂ nanosheets were transformed to WO_x, the change of the in-plane

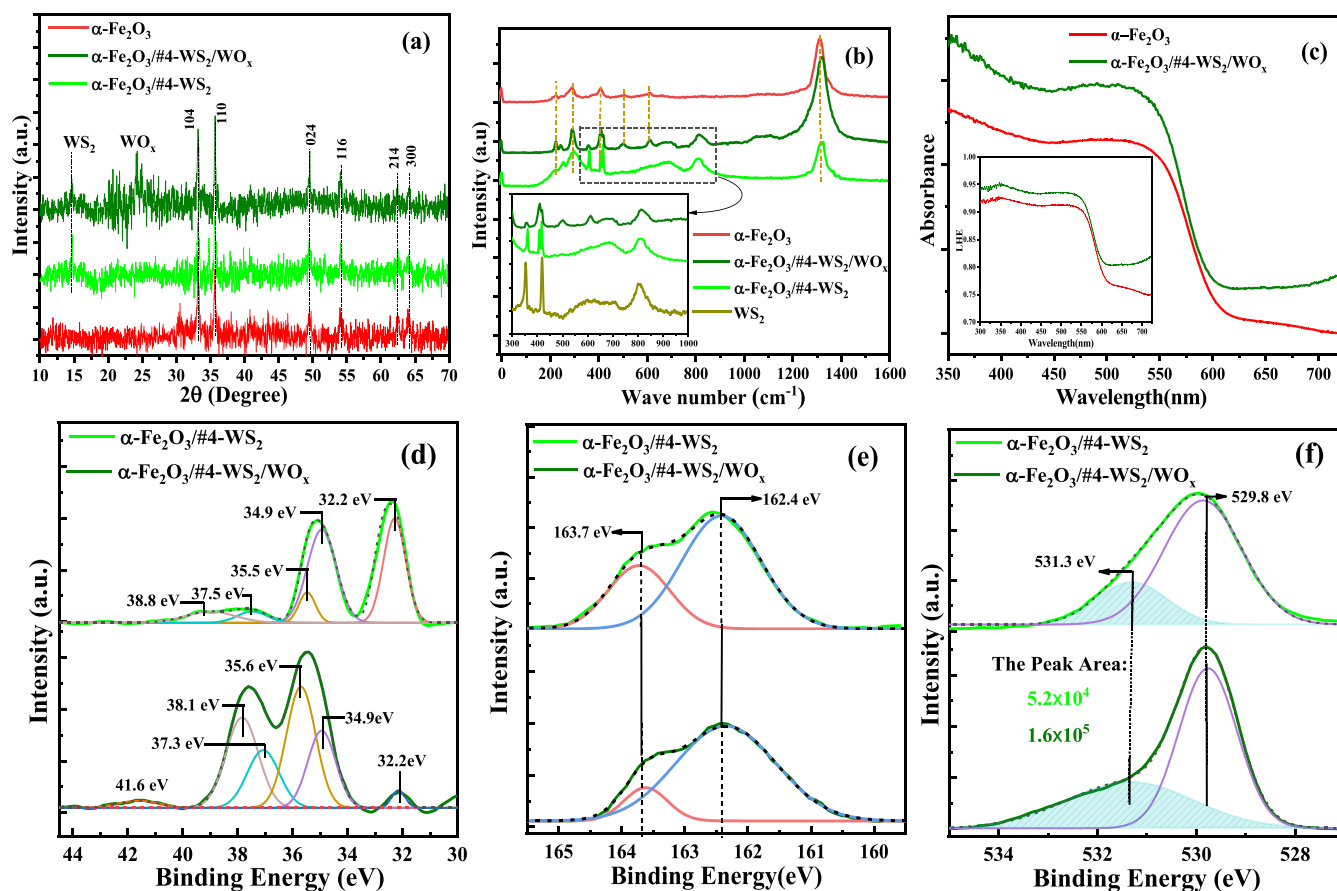


Fig. 3. a) HRXRD, b) Raman spectra, c) UV-vis absorbance (inside LHE), and high-resolution XPS spectra for d) W4f, e) S2p, and f) O1s for α -Fe₂O₃/#4-WS₂ and α -Fe₂O₃/#4-WS₂/WO_x photoelectrode.

Table 1Amount of WS₂ nanosheets on the α -Fe₂O₃ photoelectrode.

Sample's Name	Time of Drops	Volume of WS ₂ precursor: 0.1 mL \times Times of drop	Concentration of WS ₂ nanosheets in precursor (mg/mL)	Amount of WS ₂ nanosheets on each photoelectrode (mg)	Amount of WS ₂ nanosheets in photoelectrode's area (mg/cm ²) (FTOarea = 25 mm \times 25 mm)
α -Fe ₂ O ₃ /#2-WS ₂ /WO _x	2	2 \times 0.1 = 0.2	0.04	0.008	0.0013
α -Fe ₂ O ₃ /#4-WS ₂ /WO _x	4	4 \times 0.1 = 0.4	0.04	0.016	0.0026
α -Fe ₂ O ₃ /#8-WS ₂ /WO _x	8	8 \times 0.1 = 0.8	0.04	0.032	0.0051

mode may result from the strain experienced during the drop-casting and annealing process. Thus, transformation of WS₂ may cause a slight shift of the Raman peaks in the α -Fe₂O₃/#4-WS₂/WO_x sample [35,36].

UV-vis absorption spectra were evaluated for α -Fe₂O₃ and α -Fe₂O₃/#4-WS₂/WO_x thin films (Fig. 3c). The absorbance of α -Fe₂O₃/#4-WS₂/WO_x thin film as compared with that of the bare α -Fe₂O₃ was moderately enhanced by loading the WS₂ shell on the α -Fe₂O₃ thin film. Further, absorbance and bandgap energies of pure α -Fe₂O₃ and pure WS₂ photoanodes are shown in Figs. S4a and S4b, respectively. Bandgaps of the prepared α -Fe₂O₃ and WS₂ were estimated by Tauc equation (Eq. S1). Schematic electronic band structure of α -Fe₂O₃ and WS₂ before and after heterojunction were studied by UPS spectra (Fig. S5). These band alignment in the core-shell α -Fe₂O₃/#4-WS₂/WO_x structure revealed higher optical absorbance under visible light as compared with that of the bare α -Fe₂O₃ thin film due to increase of charge separation and simultaneous facilitation of charge transfer [37]. The light-harvesting efficiency (LHE) of the α -Fe₂O₃/#4-WS₂/WO_x thin film showed an enhancement of light absorption which would be effective to catch more photons and generate more charge carriers. As shown in Fig. 3c, the LHE is given by Eq. (6) [38]:

$$\text{LHE} = 1 - 10^{-A(\lambda)} \quad (6)$$

where $A(\lambda)$ is the absorbance in various wavelengths. Therefore, the enhanced absorbance of α -Fe₂O₃/#4-WS₂/WO_x electrode caused greater LHE quantities. The LHE improvement can be attributed to the fact that the combination of WS₂ nanosheets with α -Fe₂O₃ through heterojunction has a notable supplementary effect on optical properties. In addition, WS₂ nanosheets as a shell play a key role to enhance light absorption efficiency [39].

X-ray photoelectron spectroscopy (XPS) spectra were measured for α -Fe₂O₃, α -Fe₂O₃/#4-WS₂, and α -Fe₂O₃/#4-WS₂/WO_x thin films to determine elemental compositions on the surface (Figs. 3d–3f and S6). The survey spectrum shown in Fig. S6e indicated the presence of elements on the surface of the prepared α -Fe₂O₃, α -Fe₂O₃/#4-WS₂, and α -Fe₂O₃/#4-WS₂/WO_x electrodes. Carbon contamination and adventitious carbon from the XPS equipment appeared as C1s peak at 284.8 eV (Fig. S6e). XPS spectra of α -Fe₂O₃ and α -Fe₂O₃/#4-WS₂/WO_x thin films revealed two main peaks for Fe2p (Figs. S6a, S6b, and S6c). The spectra could be deconvoluted into six peaks at around 709, 711, 717, 723, 726, and 732 eV. Peaks around 709 and 711 eV for Fe (2p_{3/2}) and peaks of 723 and 726 eV of Fe (2p_{1/2}) for α -Fe₂O₃, α -Fe₂O₃/#4-WS₂, and α -Fe₂O₃/#4-WS₂/WO_x samples can be assigned to different oxidation states of iron, FeO, and Fe₂O₃, respectively (Figs. S6a, S6b, and S6c). Two Fe (2p_{3/2}) satellite and Fe (2p_{1/2}) satellite peaks showed binding energies around 717 eV and 732 eV, respectively, which were related to the Fe³⁺ oxidation state of Fe (2p_{1/2}) and Fe (2p_{3/2}) [40]. The binding energies of Fe 2p_{3/2} and Fe 2p_{1/2} peaks were slightly shifted to the lower values in α -Fe₂O₃/#4-WS₂, and α -Fe₂O₃/#4-WS₂/WO_x photoanodes as compared with that of the bare α -Fe₂O₃ thin film, which confirm the electron migration path from the WS₂/WO_x to α -Fe₂O₃ at II-type heterojunction [41]. In α -Fe₂O₃/#4-WS₂ and

α -Fe₂O₃/#4-WS₂/WO_x samples, two additional sets of peaks are detected for tungsten. These peaks demonstrate the presence of a partially increased amount of WO_x (37.9 and 35.8 eV) in Fig. 3d, as well as oxygen-free tungsten in the 4⁺ valence state (32.2 and 34.9 eV), as expected for WS₂. Peaks related to the WO_x with 5⁺ and 6⁺ valence at α -Fe₂O₃/#4-WS₂ sample are considerably lower than that of α -Fe₂O₃/#4-WS₂/WO_x electrode, which is indicative of partially increased WO_x on the surface [42,43]. As shown in Fig. 3e, the binding energies of two S2p peaks that appeared at approximately 162.4 eV originates from S 2p_{3/2}, and the other peak at 163.6 eV which represents S 2p_{1/2}. [44]. Fig. 3f presents the peak located at 529.8 eV originated from the lattice oxygen anions, while the species of O1s located at 531.4 eV belongs to the oxygen vacancies on the surface of the α -Fe₂O₃, α -Fe₂O₃/#4-WS₂, and α -Fe₂O₃/#4-WS₂/WO_x samples (Fig. 3f and S6d) [45]. An obvious enhancement of O1s located at 531.4 eV peak area in α -Fe₂O₃/#4-WS₂/WO_x photoanode proves that the fabricated α -Fe₂O₃/#4-WS₂/WO_x photoanode with annealing process has a higher concentration of surface oxygen vacancies compared with that of α -Fe₂O₃/#4-WS₂ and pure α -Fe₂O₃ electrodes [46].

Oxygen vacancy densities of pure α -Fe₂O₃ and α -Fe₂O₃/#4-WS₂/WO_x samples were investigated using EPR spectra analysis (Fig. S10). The intensity of paramagnetic signals showed a significant increase after making heterojunction. These results convincingly showed that the α -Fe₂O₃/#4-WS₂/WO_x electrode had more defects than the pure α -Fe₂O₃ electrode. Furthermore, g values for the pure α -Fe₂O₃ and α -Fe₂O₃/#4-WS₂/WO_x photoanodes were detected at around 2.002 and 1.989, respectively. The g value shifted to a lower number, which might be related to electron-poor capacitance and higher oxidation reaction. Particularly, the ESR result indicated the existence of sulfur vacancies as anion could provide unpaired electrons, which could also improve photoelectrochemical performance for the oxidation reaction. Thus, the ultrathin WS₂ shells on the surface of α -Fe₂O₃ nanorods facilitated the hole transfer to the α -Fe₂O₃/#4-WS₂/WO_x electrode/electrolyte interface and enhanced oxidation reactions [47].

Time-of-flight secondary ion mass spectrometry (TOF-SIMS) of the α -Fe₂O₃/#4-WS₂ and α -Fe₂O₃/#4-WS₂/WO_x samples were investigated to obtain details about depth, surface, and interface (Fig. 4, S7, S8, and S9). The TOF-SIMS surface analysis of the α -Fe₂O₃/#4-WS₂/WO_x electrode was performed in negative and positive polarity in the 0–300 mass range to find the reason for high electrode stability in alkaline solution in the presence of sulfur vacancies. The presence of WO₄, WO₃, WO₂, WO WS₂, and WS ions on the surface of α -Fe₂O₃/#4-WS₂ and α -Fe₂O₃/#4-WS₂/WO_x electrodes in the form of the surface and three-dimensional images is shown in Fig. 4a–f and S7. The evidence clearly confirmed the existence of the W-O, S-W-O, and W-S binding at outer surfaces (Fig. 4c–f). The peak area related to WS₂, WS, WO, and W positive ions shows that the most positive species coexist on the surface of the α -Fe₂O₃/#4-WS₂ photoanode. Furthermore, the WS₂ nanosheets were also changed into WO₄, WO₃, and WO₂ negative ions on the surface of the α -Fe₂O₃/#4-WS₂/WO_x photoanode during the calcination process in a furnace at 450°C. The highest amount of area allocated to WO₄ and WO₃ negative ions confirmed that an amount of WO_x from oxidized WS₂ nanosheets was created on the outer surface of the α -Fe₂O₃/#4-

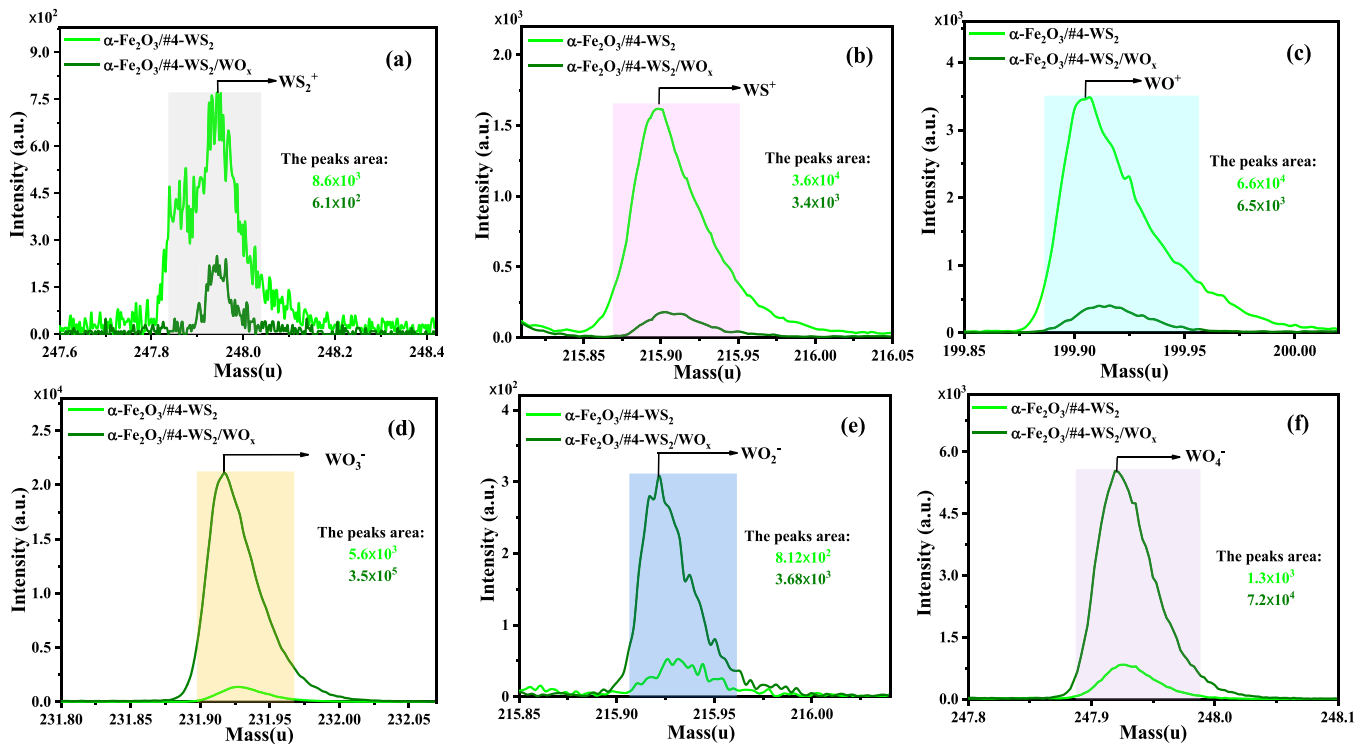


Fig. 4. TOF-SIMS. Surface analysis for the positive a) WS₂, b) WS, and c) WO ions, and negative d) WO₃, e) WO₂, and f) WO₄ ions of the $\alpha\text{-Fe}_2\text{O}_3/\#4\text{-WS}_2$ and $\alpha\text{-Fe}_2\text{O}_3/\#4\text{-WS}_2/\text{WO}_x$ electrodes.

WS₂/WO_x photoanode. The ion intensities were detected as a function of sputtering time in-depth profile analysis (Figs. S9e and S9f). Note that WO₄, WO₃, WO₂, WO, WS₂, and WS ion intensities have almost been the

same by increasing the sputtering time, implying that WS₂ was evenly distributed in a form of homogeneous shell that covered the $\alpha\text{-Fe}_2\text{O}_3/\#4\text{-WS}_2/\text{WO}_x$ nanorod structure. Further, the heat treatment process

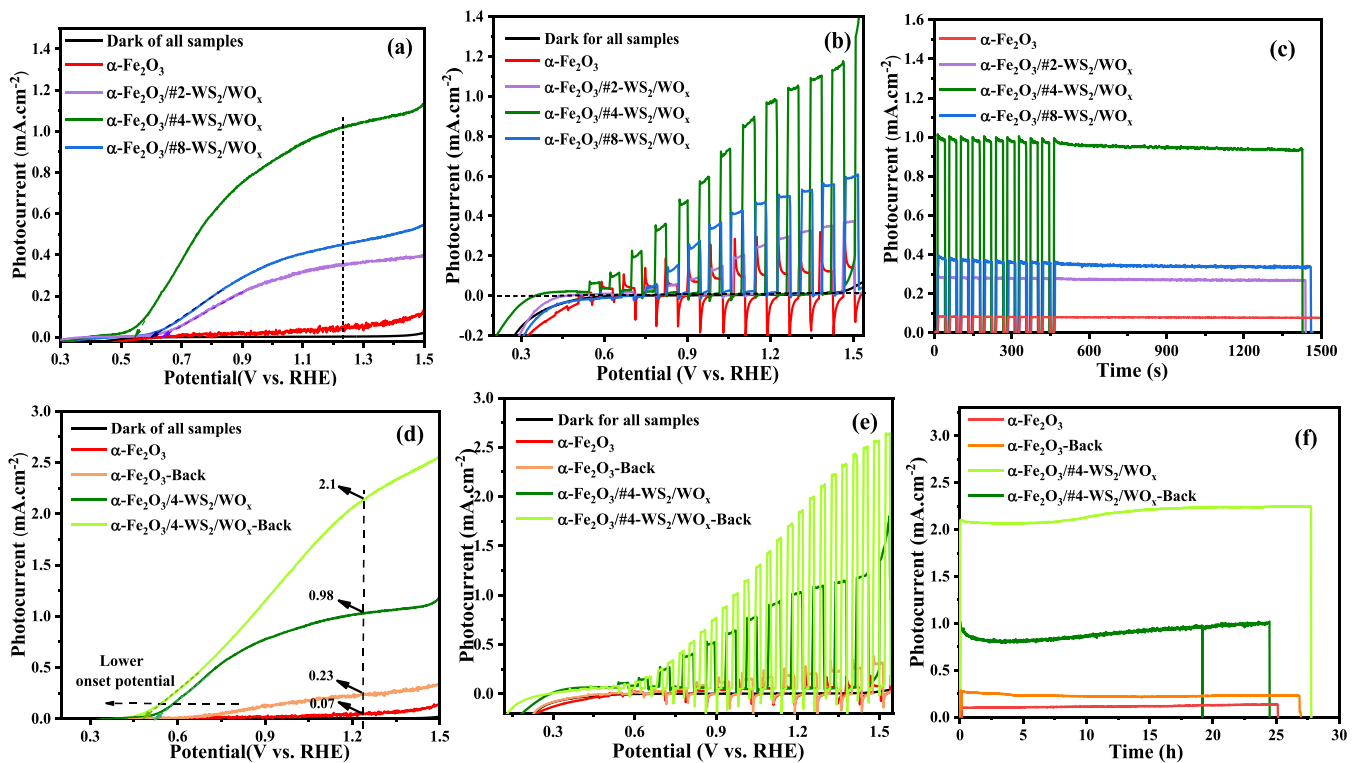


Fig. 5. a) Linear scan voltammetry (LSV) and b) Chopped LSV at potentials from 0.3–1.5 V_{RHE}, c) Photocurrent response and stability at 1.23 V_{RHE} of $\alpha\text{-Fe}_2\text{O}_3$, $\alpha\text{-Fe}_2\text{O}_3/\#2\text{-WS}_2/\text{WO}_x$, $\alpha\text{-Fe}_2\text{O}_3/\#4\text{-WS}_2/\text{WO}_x$, and $\alpha\text{-Fe}_2\text{O}_3/\#8\text{-WS}_2/\text{WO}_x$ photoanodes. d) LSV, e) Chopped LSV at potentials from 0.3 V to 1.5 V vs. RHE, f) long-term stability at 1.23 V vs. RHE for $\alpha\text{-Fe}_2\text{O}_3$ and $\alpha\text{-Fe}_2\text{O}_3/\#4\text{-WS}_2/\text{WO}_x$ samples under front- and back-side illumination.

was made the SO_x anionic groups in the structure. The TOF-SIMS and XPS analysis for $\alpha\text{-Fe}_2\text{O}_3/\#4\text{-WS}_2$ (heat treatment at 90°C) and $\alpha\text{-Fe}_2\text{O}_3/\#4\text{-WS}_2/\text{WO}_x$ (heat treatment at 450°C) electrodes also demonstrate the coexistent for sulfur oxides anions (SO_4 , SO_3 , and SO_2 negative ions) at the surface of photoanodes (Figs. S9a-S9d) [48]. Complicated structures where oxygen and sulfur are found together in one framework, often result in structures with important physical properties. Due to the different charge numbers and geometry configurations, anions (A^-) demonstrated various capabilities to enhance the charge separation as compared to that of pure $\alpha\text{-Fe}_2\text{O}_3$ electrode. Based on these observations, it is probable that the OER performance of $\alpha\text{-Fe}_2\text{O}_3/\#4\text{-WS}_2/\text{WO}_x$ (heat treatment at 450°C) electrode can be efficiently modified by the interlayer anions and enhanced the internal static electric field at the space charge layer [49,50]. Hence, after adding WS_2 nanosheets on the $\alpha\text{-Fe}_2\text{O}_3$ thin film, an amount of WO_x from the oxidized WS_2 was created on the top layer of the photoelectrode. These results confirmed that the high long-term stability of the alkaline-weak- WS_2 on the surface of the $\alpha\text{-Fe}_2\text{O}_3$ photoanode was due to the formation of WO_x on the top surface as a thin layer to enhance PEC water splitting for efficient oxygen evolution reaction.

3.3. The PEC performance of photoelectrodes

The photocurrent density vs. potential was investigated for $\alpha\text{-Fe}_2\text{O}_3$, $\alpha\text{-Fe}_2\text{O}_3/\#n\text{-WS}_2$, and all $\alpha\text{-Fe}_2\text{O}_3/\#n\text{-WS}_2/\text{WO}_x$ electrodes through linear scan voltammetry (LSV) (Fig. 5a and S13a) and chopped LSV for $\alpha\text{-Fe}_2\text{O}_3$ and all $\alpha\text{-Fe}_2\text{O}_3/\#n\text{-WS}_2/\text{WO}_x$ electrodes between 0.3 and 1.5 V_{RHE} in 1 M NaOH solution as an electrolyte (Fig. 5b). The photocurrent density for the pure $\alpha\text{-Fe}_2\text{O}_3$ electrode was $\sim 0.07\text{ mA cm}^{-2}$ at 1.23 V_{RHE} . After deposition of the WS_2 nanosheets on the $\alpha\text{-Fe}_2\text{O}_3$ electrode, the highest photocurrent density was 0.98 mA cm^{-2} at 1.23 V_{RHE} for the $\alpha\text{-Fe}_2\text{O}_3/\#4\text{-WS}_2/\text{WO}_x$ photoanode (Fig. 5a). The photocurrent density of the core-shell $\alpha\text{-Fe}_2\text{O}_3/\#4\text{-WS}_2/\text{WO}_x$ increased 13-fold using a heterojunction between $\alpha\text{-Fe}_2\text{O}_3$ and WS_2 . The enhanced photocurrent density at the modified electrodes can be attributed to the

increasing anions and oxygen vacancies, which are thought to be an energetic trap for photogenerated holes to increase the majority carrier density and hence the conductivity. Therefore, this structure simultaneously enhanced the charge separation and decreased the recombination of charge carriers [51]. However, additional amount of WS_2 loaded on the $\alpha\text{-Fe}_2\text{O}_3$ significantly reduced photocurrent density values. This reduction might be related to the fact that excessive WS_2 can block the light absorption of the photoanode [52]. Interestingly, heterojunction of WS_2 nanosheets on the surface of $\alpha\text{-Fe}_2\text{O}_3$ photoanode with calcination process significantly decreased the onset potential to a lower applied voltage (0.47 V_{RHE}). The photocurrent density and onset potential values for all prepared photoelectrodes are clearly compared as shown in Fig. 6f. The chopped LSV in Fig. 5b was measured under 2 s light on/off, consistent with LSV results (Fig. 5a). This confirmed that the core-shell $\alpha\text{-Fe}_2\text{O}_3/\#4\text{-WS}_2/\text{WO}_x$ nanorod structure as a promise photoanode could quickly react to the light and rapidly generate photocurrent from zero to its equilibrium value [53].

The amount of photocurrent density relies on lots of circumstances, containing the direction of light illumination. The photocurrent density under the back-side illumination was significantly increased compared to that front-side illumination (Fig. 5d and e). As shown in Fig. 5d, the photocurrent density for $\alpha\text{-Fe}_2\text{O}_3/\#4\text{-WS}_2/\text{WO}_x$ photoanode identifies $\sim 2.1\text{ mA cm}^{-2}$, which is approximately 30 and 2 times higher than that for the pure $\alpha\text{-Fe}_2\text{O}_3$ and $\alpha\text{-Fe}_2\text{O}_3/\#4\text{-WS}_2/\text{WO}_x$ under front-side illumination, respectively. The schematic picture shown in Fig. S14 demonstrates the separation of electron-hole pairs near the FTO, leading to better collection and transfer for electrons under back-side illumination for $\alpha\text{-Fe}_2\text{O}_3/\#4\text{-WS}_2/\text{WO}_x$. Thus, the lower distance to FTO has been led to near light-absorption depth and improved the carrier diffusion length in the $\alpha\text{-Fe}_2\text{O}_3$ and $\alpha\text{-Fe}_2\text{O}_3/\#4\text{-WS}_2/\text{WO}_x$ photoanodes [54]. Table S4 summarizes experimental conditions and photoelectrochemical performances of recently reported heterojunction $\alpha\text{-Fe}_2\text{O}_3$ with TMD or 2D materials. To the best of our knowledge, heterojunction WS_2 with $\alpha\text{-Fe}_2\text{O}_3$ photoanode has not been reported yet. Our work on photocurrent and onset potential of heterojunction WS_2 with $\alpha\text{-Fe}_2\text{O}_3$

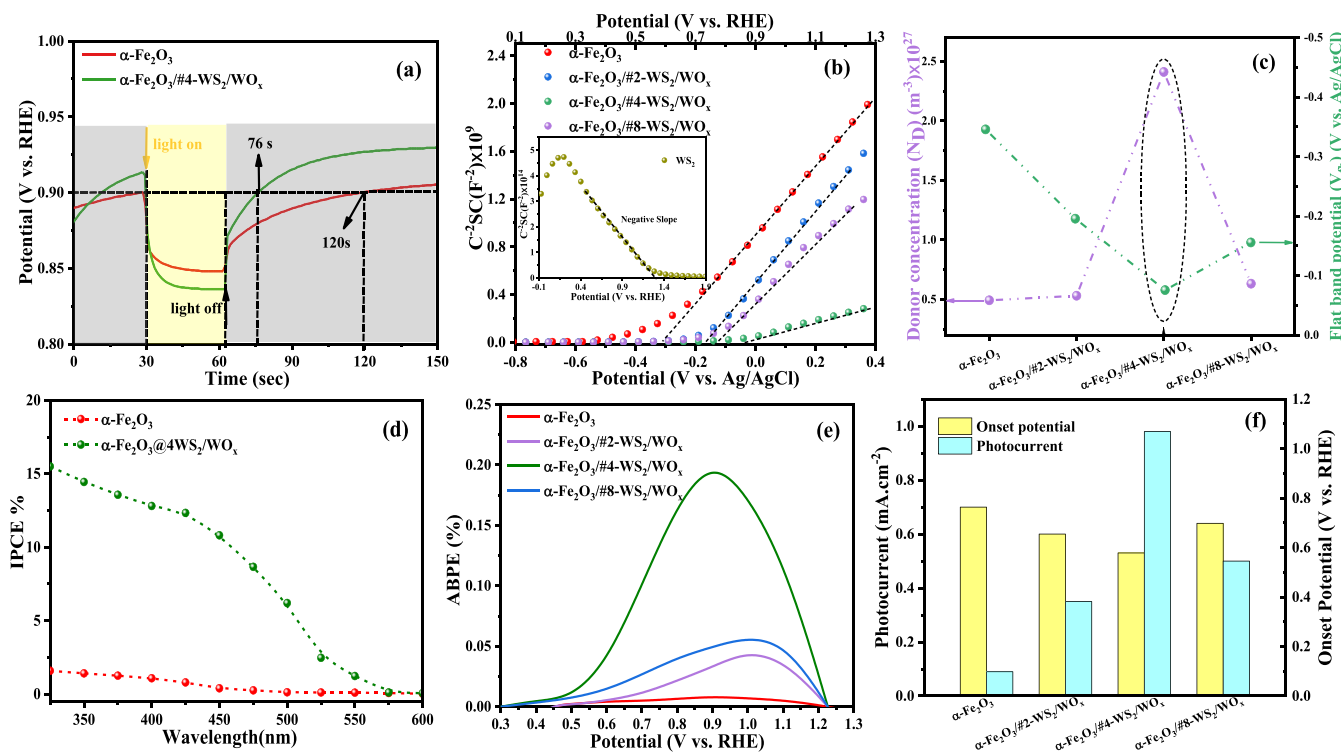


Fig. 6. a) OCP, b) Mott-Schottky, c) relationship between N_D and V_{fb} , and d) IPCE e) ABPE, and f) observed current density at 1.23 V vs. RHE and onset potentials plots for $\alpha\text{-Fe}_2\text{O}_3$ and $\alpha\text{-Fe}_2\text{O}_3/\#n\text{-WS}_2/\text{WO}_x$ electrodes.

photoanode showed a great performance, long-term stability, and good durability, indicating that heterojunction WS_2 with $\alpha\text{-Fe}_2\text{O}_3$ photoanode can be used as a promising photoanode for future applications.

Fig. 5c shows chronoamperometry scanned for ten cycles under intermittent light irradiation (light on/off). The identical response to light on and off interval indicated a good reproducibility of the $\alpha\text{-Fe}_2\text{O}_3$, $\alpha\text{-Fe}_2\text{O}_3/\#2\text{-WS}_2/\text{WO}_x$, $\alpha\text{-Fe}_2\text{O}_3/\#4\text{-WS}_2/\text{WO}_x$, and $\alpha\text{-Fe}_2\text{O}_3/\#8\text{-WS}_2/\text{WO}_x$ photoanodes. Stabilities of photocurrent for different $\alpha\text{-Fe}_2\text{O}_3$ and $\alpha\text{-Fe}_2\text{O}_3/\#n\text{-WS}_2/\text{WO}_x$ samples were measured under continuous illumination (Fig. 5c). All prepared photoelectrodes showed stable photocurrent without showing any significant downturn in 5 h (Fig. S13c). The role of WS_2 is to enhance the PEC performance of $\alpha\text{-Fe}_2\text{O}_3$ but is not stable (Fig. S13b shows the stability of the $\alpha\text{-Fe}_2\text{O}_3/\#4\text{-WS}_2$ electrode). While we prepared $\alpha\text{-Fe}_2\text{O}_3/\#n\text{-WS}_2/\text{WO}_x$ (heat treatment at 450°C) electrode due to the higher annealing temperature produced more anions (Fig. 4 and S9), which critically influence the electronic structure, separation, and transfer of photogenerated electron and hole, and modified surface absorption. Therefore, annealing temperatures have been led to significantly enhanced stable and efficient photoelectrochemical performance of the $\alpha\text{-Fe}_2\text{O}_3/\#4\text{-WS}_2/\text{WO}_x$

photoanode. Furthermore, under front- and back-side continuous illumination for 24 h, photocurrent of $\alpha\text{-Fe}_2\text{O}_3/\#4\text{-WS}_2/\text{WO}_x$ photoanode showed good stabilities (Fig. 5f). Based on the evidence, the enhanced photocurrent density in $\alpha\text{-Fe}_2\text{O}_3/\#4\text{-WS}_2/\text{WO}_x$ photoanode is attributed to the increased light absorption (Fig. 3c), the slower recombination rate of photo-generated electron-hole pairs (Fig. 7d), and the increase in the donor concentration (Fig. 6c). Furthermore, the post-annealing temperature has a drastic effect on the PEC performance of the $\alpha\text{-Fe}_2\text{O}_3/\#4\text{-WS}_2/\text{WO}_x$ photoanode. Higher annealing temperature produced more anions (Fig. 4 and S9), which effect on the charge transfer at the interface of the $\alpha\text{-Fe}_2\text{O}_3/\#4\text{-WS}_2/\text{WO}_x$ photoanode [55].

The long-term (24 h) stability was investigated for the $\alpha\text{-Fe}_2\text{O}_3/\#4\text{-WS}_2/\text{WO}_x$ electrode (Fig. S15a). The $\alpha\text{-Fe}_2\text{O}_3/\#4\text{-WS}_2/\text{WO}_x$ electrode after 24 h of illumination showed outstanding stability and photocurrent response without significant decrease in the photocurrent density value. Furthermore, physiochemical, and morphological properties of photoelectrodes were evaluated to examine the durability of $\alpha\text{-Fe}_2\text{O}_3/\#4\text{-WS}_2/\text{WO}_x$ photoanode after continuous illumination. Results revealed no change in XPS survey after photostability experiments (Fig. S15b) or SEM results for the $\alpha\text{-Fe}_2\text{O}_3/\#4\text{-WS}_2/\text{WO}_x$ electrode after

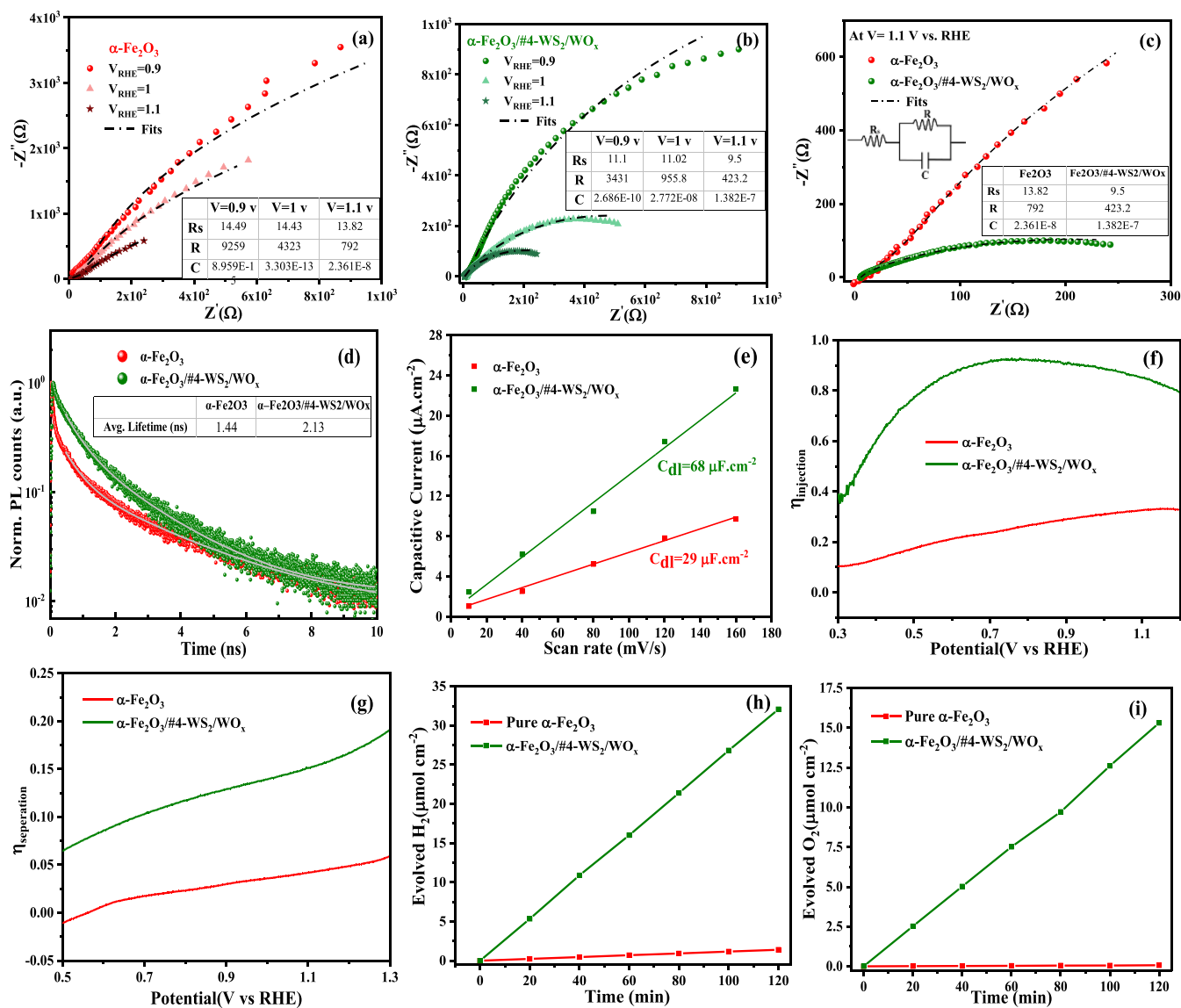


Fig. 7. Nyquist plots for a) $\alpha\text{-Fe}_2\text{O}_3$ and b) $\alpha\text{-Fe}_2\text{O}_3/\#4\text{-WS}_2/\text{WO}_x$ at potentials of 0.9, 1, and 1.1 V_{RHE} . c) Nyquist plot at potentials of 1.1 V_{RHE} , and d) TRPL for $\alpha\text{-Fe}_2\text{O}_3$ and $\alpha\text{-Fe}_2\text{O}_3/\#4\text{-WS}_2/\text{WO}_x$ electrodes. e) Electrochemical double-layer capacity (C_{dl}), f) Charge injection, g) Charge separation efficiencies, h) H_2 and i) O_2 evolution vs. reaction time per illuminated area (1 cm^2) for $\alpha\text{-Fe}_2\text{O}_3$ and $\alpha\text{-Fe}_2\text{O}_3/\#4\text{-WS}_2/\text{WO}_x$ electrodes at a potential of 1.23 V_{RHE} .

a 24 h photoreaction (Figs. S15c and S15d), suggesting that the $\alpha\text{-Fe}_2\text{O}_3/\#4\text{-WS}_2/\text{WO}_x$ photoanode was intrinsically stable for the PEC reaction.

Photogenerated charge carrier behavior was investigated in more detail using the open circuit photovoltage (OCP) measurement (Fig. 6a). In the ΔOCP plot, the lower potential at the illumination time represents more photogenerated electrons production and higher conductivity. Photoelectrodes had a negative voltage after turning on the lamp, indicating the direction of photogenerated electrons to the FTO. This confirmed the anodic photocurrent in other photoelectrochemical analyses. Furthermore, the $\alpha\text{-Fe}_2\text{O}_3/\#4\text{-WS}_2/\text{WO}_x$ photoanode took about 44 s shorter to come back to the dark equilibrium from illuminated states. It can be attributed to the lifetime of photogenerated charge carriers that noticeably prolonged after fabricating heterojunction. Therefore, the conductivity of the core-shell $\alpha\text{-Fe}_2\text{O}_3/\#4\text{-WS}_2/\text{WO}_x$ nanorod structure was increased due to increased concentration available photogenerated electrons as well as decreased recombination of charge carriers on the $\alpha\text{-Fe}_2\text{O}_3/\#4\text{-WS}_2/\text{WO}_x$ photoelectrode [56].

The Mott-Schottky (MS) plot is shown in Fig. 6b. The $\alpha\text{-Fe}_2\text{O}_3$, $\alpha\text{-Fe}_2\text{O}_3/\#2\text{-WS}_2/\text{WO}_x$, $\alpha\text{-Fe}_2\text{O}_3/\#4\text{-WS}_2/\text{WO}_x$, and $\alpha\text{-Fe}_2\text{O}_3/\#8\text{-WS}_2/\text{WO}_x$ photoanodes demonstrated positive slopes before and after heterojunction, implying properties of n-type semiconductors having electrons as charge carriers. MS parameters such as flat band potential (V_{fb}), width of the space charge region (W_{SCL}), and electron density in the conduction band (N_D) were calculated by equations S5, S6, and S7 in supporting information, respectively. Based on the following relationship for $\alpha\text{-Fe}_2\text{O}_3$, $\alpha\text{-Fe}_2\text{O}_3/\#2\text{-WS}_2/\text{WO}_x$, $\alpha\text{-Fe}_2\text{O}_3/\#4\text{-WS}_2/\text{WO}_x$, and $\alpha\text{-Fe}_2\text{O}_3/\#8\text{-WS}_2/\text{WO}_x$ photoanodes, values are summarized in Table S2. As shown in Fig. 6b, slopes of MS curves were significantly decreased, which could be attributed to the increased electron density in the conduction band and the enhanced charge carrier separation in the $\alpha\text{-Fe}_2\text{O}_3/\#4\text{-WS}_2/\text{WO}_x$ thin film by optimum shell thickness [57]. Furthermore, the calculated donor concentration (N_D) and flat band potential (V_{fb}) information as a function of the WS_2 dropping on the surface of the $\alpha\text{-Fe}_2\text{O}_3$ shows in Fig. 6c. The optimum amount of WS_2 ($\alpha\text{-Fe}_2\text{O}_3/\#4\text{-WS}_2/\text{WO}_x$) increased N_D and made a positive shift V_{fb} . However, higher WS_2 content on the surface of the $\alpha\text{-Fe}_2\text{O}_3/\#8\text{-WS}_2/\text{WO}_x$ photoanode decreased N_D and a negative shift in V_{fb} . This negative shift in V_{fb} at $\alpha\text{-Fe}_2\text{O}_3/\#8\text{-WS}_2/\text{WO}_x$ electrode may be due to the development of more defects with further increase in the WS_2 content which acted as traps for electron and holes and thus functioned as recombination centers [51].

The best value of W_{SCL} in the $\alpha\text{-Fe}_2\text{O}_3/\#4\text{-WS}_2/\text{WO}_x$ sample decreased to 2.52 nm, which was around 49% that of pure $\alpha\text{-Fe}_2\text{O}_3$ (5.18 nm). This confirmed an improvement in PEC performance by enhancing the charge carrier transfer [57]. A model that considered the geometry of $\alpha\text{-Fe}_2\text{O}_3$ and $\alpha\text{-Fe}_2\text{O}_3/\#4\text{-WS}_2/\text{WO}_x$ photoanodes and their differences with the standard flat model was developed as shown in the form of curved MS plots. Results are discussed in the supporting information. The photoanodes followed the developed model for MS plots, with a curved shape for cylindrical geometry, indicating that the whole cylindrical surface was active. Therefore, this system can be applied to improve the effective surface in the design of electronic devices (Fig. S12).

Photoelectrochemical performances of all photoanodes under visible light region irradiation were supported by incident-photon-to-current-efficiencies (IPCE) measurement using Eq. (7) [58].

$$IPCE, \% = \left(\frac{1240}{\lambda} \times \frac{J_{light}}{P_{light}} \right) \times 100 \quad (7)$$

The highest IPCE values at 325 nm for the $\alpha\text{-Fe}_2\text{O}_3$ and $\alpha\text{-Fe}_2\text{O}_3/\#4\text{-WS}_2/\text{WO}_x$ photoanodes were 1.65% and 15.5%, respectively (Fig. 6d). These highest IPCE values better support the heterojunction effect with WS_2 nanosheets. The identified IPCE for $\alpha\text{-Fe}_2\text{O}_3/\#4\text{-WS}_2/\text{WO}_x$ photoanode was 9.4-fold more than that of pure $\alpha\text{-Fe}_2\text{O}_3$. This enhanced IPCE curve corresponded to the better result of the optical absorption analysis

spectrum for $\alpha\text{-Fe}_2\text{O}_3/\#4\text{-WS}_2/\text{WO}_x$ sample under visible light [59]. Therefore, the $\alpha\text{-Fe}_2\text{O}_3/\#4\text{-WS}_2/\text{WO}_x$ photoanode can extremely improve the PEC capacity of $\alpha\text{-Fe}_2\text{O}_3$ based photoanodes in the absence of any hole scavenger [60].

Applied bias photon-to-current conversion efficiency (ABPE) under various applied potentials shown in Fig. 6f can be calculated using Eq. (8) [61].

$$ABPE(\%) = \left(\frac{J \left(\frac{\text{mA}}{\text{cm}^2} \right) \times (1.23 - V_b)(V)}{P \left(\frac{\text{mW}}{\text{cm}^2} \right)} \right) \quad (8)$$

where P is the power density of the incident light ($100 \text{ mW}/\text{cm}^2$), V_b is an applied bias vs. RHE, and J is the photocurrent density at various applied potentials. ABPE values of $\alpha\text{-Fe}_2\text{O}_3/\#n\text{-WS}_2/\text{WO}_x$ electrodes are greater than those of the $\alpha\text{-Fe}_2\text{O}_3$ over the measured potential range in 1 M NaOH as an electrolyte (Fig. 6f). The highest efficiency was evidently obtained for the $\alpha\text{-Fe}_2\text{O}_3/\#4\text{-WS}_2/\text{WO}_x$ electrode (0.194%) at the lowest potential ($0.9 V_{RHE}$), which was 19.4-fold more than that of the $\alpha\text{-Fe}_2\text{O}_3$ of 0.01%. Thus, the $\alpha\text{-Fe}_2\text{O}_3/\#4\text{-WS}_2/\text{WO}_x$ photoanode showed the highest PEC water splitting among the prepared $\alpha\text{-Fe}_2\text{O}_3$ based photoelectrodes.

The electrochemical impedance spectroscopy (EIS) of the $\alpha\text{-Fe}_2\text{O}_3$ and $\alpha\text{-Fe}_2\text{O}_3/\#4\text{-WS}_2/\text{WO}_x$ photoelectrodes was measured to investigate the cause of WS_2/WO_x shell on the photogenerated electron transfer process at the $\alpha\text{-Fe}_2\text{O}_3/\text{WS}_2/\text{electrolyte}$ interface. Fig. 7a-c shows Nyquist plots at different potentials (0.9, 1.1, $1.1 V_{RHE}$) for the $\alpha\text{-Fe}_2\text{O}_3$ and $\alpha\text{-Fe}_2\text{O}_3/\#4\text{-WS}_2/\text{WO}_x$ photoelectrodes. They were fitted by a Randles circuit model (inside Fig. 7c), which contained essentially constant and small series resistance (R_s), the space charge capacitance of the $\alpha\text{-Fe}_2\text{O}_3/\text{WS}_2/\text{electrolyte}$ interface (C), and the interfacial charge transfer resistance (R). Tables inside Fig. 7a-c show space charge capacitance and resistance values, which demonstrate the highest capacitance and lowest resistance values for the $\alpha\text{-Fe}_2\text{O}_3/\#4\text{-WS}_2/\text{WO}_x$ photoanode. As indicated in tables inside of Fig. 7a and b, the charge transfer resistance is reduced by the increase of potential because of an enhancement in electron transfer rate [62]. In Fig. 7c, the $\alpha\text{-Fe}_2\text{O}_3/\#4\text{-WS}_2/\text{WO}_x$ photoanode showed the lowest semicircle diameter at voltage $1.1 V_{RHE}$, which corresponded to the interfacial charge transfer resistance of the $\alpha\text{-Fe}_2\text{O}_3/\#4\text{-WS}_2/\text{WO}_x$ photoelectrode that was significantly decreased. This behavior could be attributable to the fabrication of a core-shell shape heterojunction with WS_2 nanosheets that improved the extraction of holes and produced more anions by higher annealing temperatures. Produced more anions in the structure could be accelerated charge transfer at the interface of the $\alpha\text{-Fe}_2\text{O}_3/\#4\text{-WS}_2/\text{WO}_x$ photoanode compared to $\alpha\text{-Fe}_2\text{O}_3/\#n\text{-WS}_2$ and pure $\alpha\text{-Fe}_2\text{O}_3$ photoanodes (Fig. S13d). Consequently, the $\alpha\text{-Fe}_2\text{O}_3/\#4\text{-WS}_2/\text{WO}_x$ core-shell decreased the charge recombination at the $\alpha\text{-Fe}_2\text{O}_3$ thin film, totally consistent with the TRPL data [63].

To obtain more insights into the influence of charge migration, electron transfer properties of pure $\alpha\text{-Fe}_2\text{O}_3$ and $\alpha\text{-Fe}_2\text{O}_3/\#4\text{-WS}_2/\text{WO}_x$ were investigated by measuring PL lifetime (Fig. 7d). TRPL spectra revealed that the average decay time ($\tau_{ave} = 2.13 \text{ ns}$) of the charge carrier of $\alpha\text{-Fe}_2\text{O}_3/\#4\text{-WS}_2/\text{WO}_x$ was longer than that of pure $\alpha\text{-Fe}_2\text{O}_3$ ($\tau_{ave} = 1.44 \text{ ns}$). This significant enhancement of the estimated τ_{ave} suggests that the use of the WS_2 nanosheets as a heterojunction could lead to an efficient charge transfer between the $\alpha\text{-Fe}_2\text{O}_3$ and WS_2 semiconductors. The better separation of electron-hole pairs consequently caused a better migration of charge carriers in the $\alpha\text{-Fe}_2\text{O}_3/\#4\text{-WS}_2/\text{WO}_x$ photoanode, making a better PEC water splitting performance. This effectively suppressed charge carriers trapping at the surface of photoelectrodes and reduced the charge recombination at $\alpha\text{-Fe}_2\text{O}_3/\#4\text{-WS}_2/\text{WO}_x/\text{electrolyte}$ interfaces, thus enhancing electron injection efficiency of $\alpha\text{-Fe}_2\text{O}_3/\#4\text{-WS}_2/\text{WO}_x$ photoanode [64].

As shown in Fig. S16a and S16b, cyclic voltammograms (CV) were measured at scan rates of 10, 40, 80, 120 and $160 \text{ mV}/\text{s}$ in 1 M NaOH for $\alpha\text{-Fe}_2\text{O}_3$ and $\alpha\text{-Fe}_2\text{O}_3/\#4\text{-WS}_2/\text{WO}_x$ electrodes, respectively. Relative

electrochemical surface areas (ECSAs) of α -Fe₂O₃ and α -Fe₂O₃/#4-WS₂/WO_x samples were investigated to know active surface areas of these electrodes. The ECSA was determined by the capacitive current associated with double layer charging from the scan rate dependence of CV measurement (Fig. 7e). Double layer capacitance (C_{dl}) was estimated from the difference between the anodic current density (J_a) and the cathodic current density (J_c) at 0.8 V vs. Ag/AgCl at various scan rates. The linear slope was equal to twice the C_{dl} that could be used to show the ECSA. The C_{dl} value (Fig. 7e) for the α -Fe₂O₃/#4-WS₂/WO_x electrode was 63 $\mu\text{F cm}^{-2}$, which was higher than that of pure α -Fe₂O₃ (29 $\mu\text{F cm}^{-2}$). The higher C_{dl} value is attributed to a larger active surface area. Therefore, the modified α -Fe₂O₃/#4-WS₂/WO_x photoanode had a larger active surface area, which can be attributed to the heterostructure rich in active edge sites [65].

The electrochemical parameters anodic Tafel slopes (β_a), corrosion current density (I_{corr}), and corrosion potential (E_{corr}), were determined from the polarization curves (Tafel curves), and they are presented in Fig. S16c and Table S3. Regarding the kinetics of the electrochemical performance, which were inspected by extracting the anodic slope, those for α -Fe₂O₃/#4-WS₂/WO_x (320 mV dec⁻¹) were lowest compared to that of pure α -Fe₂O₃ (476 mV dec⁻¹). This can be attributed to the enhanced water oxidation reaction kinetics in this heterojunction-designed electrode [66].

Photocurrent generally arises through light-absorption, charge separation, and surface charge-injection for PEC performance. As shown in Fig. S11, there was a significant enhancement in the photocurrent density and the obvious shift of the onset potential in the presence of H₂O₂ for α -Fe₂O₃ and α -Fe₂O₃/#4-WS₂/WO_x photoelectrode because of a faster oxidation kinetics [67]. WS₂ nanosheets were loaded on the surface of the α -Fe₂O₃ photoanode to overcome the reaction barrier to

impressively improve the charge migration through the electrode/electrolyte interface. The surface charge injection efficiency (η_{inj}) and the charge separation efficiency (η_{sep}) of the pure α -Fe₂O₃ and the α -Fe₂O₃/#4-WS₂/WO_x photoanodes are shown in Fig. 7f and g, respectively. By loading WS₂ nanosheets as a shell on the surface of α -Fe₂O₃ nanorods, η_{inj} of the α -Fe₂O₃ increased from ca. 0.25 to ca. 0.88 at 0.6 V_{RHE}. Obviously, the η_{sep} and η_{inj} were enhanced in the core-shell the α -Fe₂O₃/#4-WS₂/WO_x nanorods by fabricating heterojunction with 2D-WS₂ nanosheets. Values of η_{sep} were ca. 0.003 to ca. 0.09 at 0.6 V_{RHE} for the pure α -Fe₂O₃ photoanode and the α -Fe₂O₃/#4-WS₂/WO_x photoanode, respectively [68].

Overall water splitting of α -Fe₂O₃, and α -Fe₂O₃/#4-WS₂/WO_x photoelectrodes was investigated by measuring H₂ and O₂ evolution at 1.23 V_{RHE} under 100 mW cm⁻² irradiations in 1 M NaOH electrolyte. As shown in Fig. 7h and i, the total H₂ generated after 2 h of irradiation for α -Fe₂O₃ and α -Fe₂O₃/#4-WS₂/WO_x photoanodes were 1.39, and 32 $\mu\text{mol.cm}^{-2}$, respectively, and the total O₂ generated were 0.69, and 15.3 $\mu\text{mol.cm}^{-2}$, respectively, indicating a 2:1 ratio of water splitting reaction. The H₂/O₂ gas evolution process was accompanied by a stable photocurrent density as presented by chronoamperometry shown in Fig. 5f. Furthermore, the Faradaic efficiency of O₂ and H₂ evolution for α -Fe₂O₃/#4-WS₂/WO_x photoanode was determined to be 82–86% (see detailed calculation process in Supporting Information part 15), indicating that most photogenerated holes were used for the water oxidation reaction [69].

The photoelectrochemical mechanism can be summarized as three steps: (I) the light-absorption by semiconductor and generate electron-hole pairs; (II) simultaneously electrons and holes transfer to the photocathode and photoanode surface, respectively; and (III) Oxidation-reduction reaction happens on the surface of the photoelectrodes to

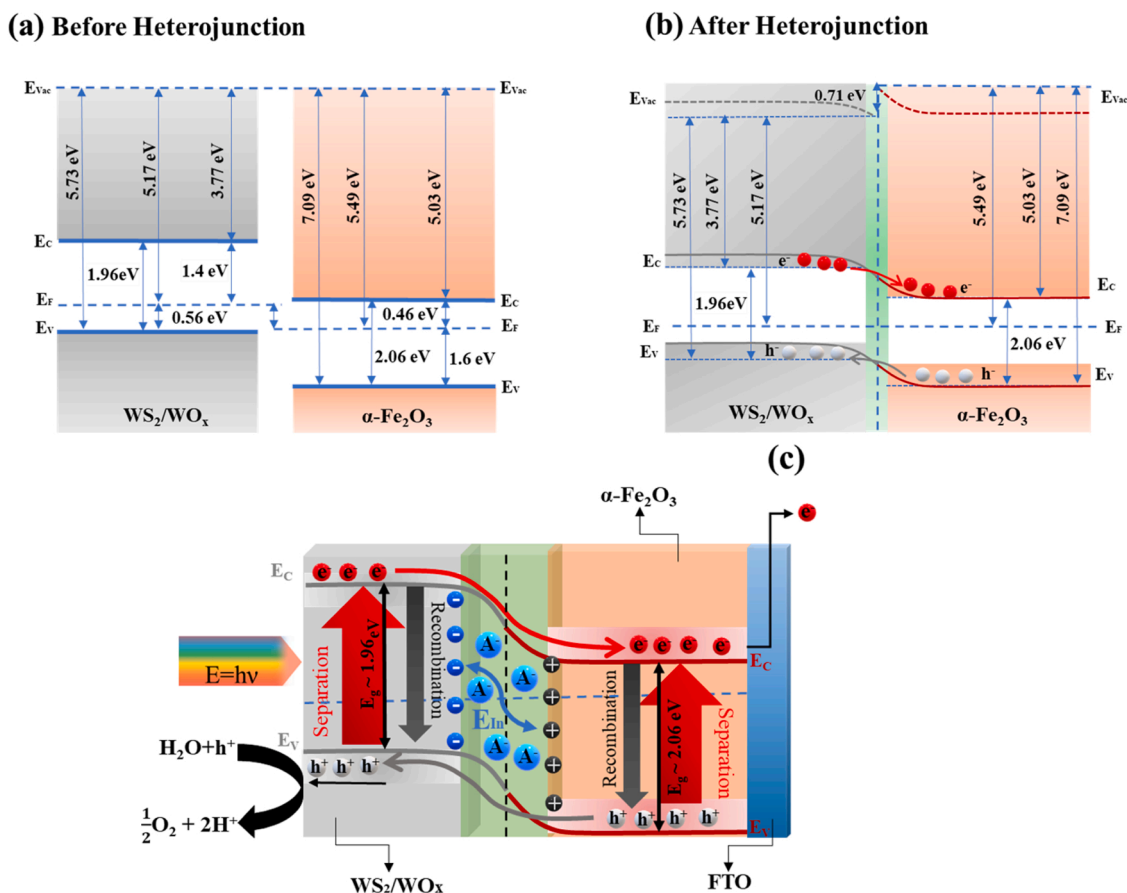


Fig. 8. Schematic electronic band structure a) before and b) after heterojunction and c) charge separation and transfer pathway at the α -Fe₂O₃ heterojunction with WS₂/WO_x.

produce hydrogen and oxygen. The energy band bending of the α -Fe₂O₃ electrode was investigated in the core-shell α -Fe₂O₃/#4-WS₂/WO_x structure before and after heterojunction in Fig. 8a and b using UPS analysis and calculating the work function (Fig. S5). The charge separation and transfer pathway at the α -Fe₂O₃ heterojunction with WS₂ schematically shows in Fig. 8. After the absorption of light energy by semiconductor, electrons in the valence band obtained energy from the visible light illumination were moved from the valence band (VB) to the conduction band (CB) in both α -Fe₂O₃ and WS₂ semiconductors. Corresponding to improved PEC performance, the charge separation increased after fabrication of the core-shell α -Fe₂O₃/#4-WS₂/WO_x nanorod structure. The recombination rate of electron-hole pairs was significantly decreased due to reduction of resistance at interfaces, thus increasing charge carrier lifetime. Furthermore, electrons can be transferred from the CB of WS₂ to the CB of α -Fe₂O₃ at different energy levels. Due to the same reason, holes simultaneously moved from the VB of α -Fe₂O₃ to the VB of WS₂ by the electrostatic field. This inner electrostatic field (E_{in}) can extract more charge carriers at the space charge region. On the other hand, anions (A^-) with higher charges at the interlayer would cause much more enhancement on the E_{in} , thus be more favorable to the separation of electron-hole pairs facilitating the transfer of hole (h^+), and finally achieve higher photocurrent [55]. As a result, the core-shell α -Fe₂O₃/#4-WS₂/WO_x nanorod structure can generate more electrons and holes on the surface of photoelectrodes, facilitate electron-hole transfer by the anions at the interlayer, leading to increased PEC performance [70].

4. Conclusion

In this work, a new heterojunction between α -Fe₂O₃ nanorods and WS₂ nanosheets was fabricated by a simple drop-casting process. Furthermore, the thickness, concentration, and temperature were optimized to obtain efficient PEC performance. The highest photocurrent density was identified for α -Fe₂O₃/#4-WS₂/WO_x electrode, which is about 13 and 30-fold higher than that of pure α -Fe₂O₃ photoelectrode. This significant enhancement in the PEC performance of the α -Fe₂O₃/#4-WS₂/WO_x photoanode can be attributed to the higher light absorption (UV-vis), and slower recombination rate of photo-generated electron-hole pairs (TRPL), and the increase in the donor concentration (Mott-Schottky). Furthermore, the post-annealing temperatures have a drastic effect on the PEC performance of the α -Fe₂O₃/#4-WS₂/WO_x photoanode. Higher annealing temperatures produced more anions (TOF-SIMS), which affect the charge transfer at the interface of the α -Fe₂O₃/#4-WS₂/WO_x photoanode. It is expected that the combination of WS₂ heterojunction and formation of WO_x of the α -Fe₂O₃/#4-WS₂/WO_x photoanode can be a good strategy for extending to the fabrication of other novel photoelectrodes for enhanced performance in the field of PEC water splitting.

CRedit authorship contribution statement

Zohreh Masoumi: Investigation, Methodology, Data curation, Writing – original draft. **Meysam Tayebi:** Conceptualization, Writing – review & editing. **Morteza Kolaei:** Acquisition and interpretation of data. **Byeong-Kyu Lee:** Supervision, Writing – review & editing, Funding acquisition.

Declaration of Competing Interest

The authors declare that they have no known competing financial interests or personal relationships that could have appeared to influence the work reported in this paper.

Acknowledgement

This work was supported by a grant (No. 2019R1A2C2085250) of the

National Research Foundation of Korea (NRF) funded by the Ministry of Science and ICT (MSIT), Republic of Korea.

Appendix A. Supporting information

Supplementary data associated with this article can be found in the online version at doi:10.1016/j.apcatb.2022.121447.

References

- [1] L. Li, et al., Ultrathin MoSe₂ nanosheet anchored CdS-ZnO functional paper chip as a highly efficient tandem Z-scheme heterojunction photoanode for scalable photoelectrochemical water splitting, *Appl. Catal. B: Environ.* 292 (2021), 120184, <https://doi.org/10.1016/j.apcatb.2021.120184>.
- [2] T. Wu, G. Deng, C. Zhen, Metal oxide mesocrystals and mesoporous single crystals: synthesis, properties and applications in solar energy conversion, *J. Mater. Sci. Technol.* 73 (2021) 9–22, <https://doi.org/10.1016/j.jmst.2020.09.025>.
- [3] M. Kolaei, M. Tayebi, B.-K. Lee, The synergistic effects of acid treatment and silver (Ag) loading for substantial improvement of photoelectrochemical and photocatalytic activity of Na₂Ti₃O₇/TiO₂ nanocomposite, *Appl. Surf. Sci.* 540 (2021), 148359, <https://doi.org/10.1016/j.apsusc.2020.148359>.
- [4] M. Tayebi, B.-K. Lee, The effects of W/Mo-co-doped BiVO₄ photoanodes for improving photoelectrochemical water splitting performance, *Catal. Today* 361 (2021) 183–190, <https://doi.org/10.1016/j.cattod.2020.03.066>.
- [5] X. Long, et al., Bamboo shoots shaped FeVO₄ passivated ZnO nanorods photoanode for improved charge separation/transfer process towards efficient solar water splitting, *Appl. Catal. B: Environ.* 257 (2019), 117813, <https://doi.org/10.1016/j.apcatb.2019.117813>.
- [6] H.-M. Li, et al., Synergetic integration of passivation layer and oxygen vacancy on hematite nanoarrays for boosted photoelectrochemical water oxidation, *Appl. Catal. B: Environ.* 284 (2021), 119760, <https://doi.org/10.1016/j.apcatb.2020.119760>.
- [7] R. Chong, et al., 2D Co-incorporated hydroxyapatite nanoarchitecture as a potential efficient oxygen evolution cocatalyst for boosting photoelectrochemical water splitting on Fe₂O₃ photoanode, *Appl. Catal. B: Environ.* 250 (2019) 224–233, <https://doi.org/10.1016/j.apcatb.2019.03.038>.
- [8] K. Dashtian, et al., A review on metal-organic frameworks photoelectrochemistry: a headlight for future applications, *Coord. Chem. Rev.* 445 (2021), 214097, <https://doi.org/10.1016/j.ccr.2021.214097>.
- [9] Z. Masoumi, et al., Simultaneous enhancement of charge separation and hole transportation in a W:α-Fe₂O₃/MoS₂ photoanode: a collaborative approach of MoS₂ as a heterojunction and W as a metal dopant, *ACS Appl. Mater. Interfaces* 13 (33) (2021) 39215–39229, <https://doi.org/10.1021/acsami.1c08139>.
- [10] S. Shen, et al., Hematite heterostructures for photoelectrochemical water splitting: rational materials design and charge carrier dynamics, *Energy Environ. Sci.* 9 (9) (2016) 2744–2775, <https://doi.org/10.1039/C6EE01845A>.
- [11] B. Klahr, et al., Photoelectrochemical and impedance spectroscopic investigation of water oxidation with “Co-Pi”-coated hematite electrodes, *J. Am. Chem. Soc.* 134 (40) (2012) 16693–16700, <https://doi.org/10.1021/ja306427f>.
- [12] A. Kudo, Y. Miseki, Heterogeneous photocatalyst materials for water splitting, *Chem. Soc. Rev.* 38 (1) (2009) 253–278, <https://doi.org/10.1039/B800489G>.
- [13] C.T. Le, et al., Effects of interlayer coupling and band offset on second harmonic generation in vertical MoS₂/MoS₂(1–x)Se_{2x} structures, *ACS Nano* 14 (4) (2020) 4366–4373, <https://doi.org/10.1021/acsnano.9b09901>.
- [14] S. Choi, et al., Vertically aligned MoS₂ thin film catalysts with Fe-Ni sulfide nanoparticles by one-step sulfurization for efficient solar water reduction, *Chem. Eng. J.* 418 (2021), 129369, <https://doi.org/10.1016/j.cej.2021.129369>.
- [15] M. Tayebi, Z. Masoumi, B.-K. Lee, Ultrasonically prepared photocatalyst of W/WO₃ nanoplates with WS₂ nanosheets as 2D material for improving photoelectrochemical water splitting, *Ultrason. Sonochem.* 70 (2021), 105339, <https://doi.org/10.1016/j.ultsonch.2020.105339>.
- [16] X. Song, J. Hu, H. Zeng, Two-dimensional semiconductors: recent progress and future perspectives, *J. Mater. Chem. C* 1 (17) (2013) 2952–2969, <https://doi.org/10.1039/C3TC00710C>.
- [17] M.A. Lukowski, et al., Highly active hydrogen evolution catalysis from metallic WS₂ nanosheets, *Energy Environ. Sci.* 7 (8) (2014) 2608–2613, <https://doi.org/10.1039/C4EE01329H>.
- [18] G. Xi, et al., Fe₃O₄/WO₃ hierarchical core-shell structure: high-performance and recyclable visible-light photocatalysis, *Chem. – A Eur. J.* 17 (18) (2011) 5145–5154, <https://doi.org/10.1002/chem.201002229>.
- [19] K.S. Novoselov, et al., 2D materials and van der Waals heterostructures, *Science* 353 (6298) (2016) aac9439, <https://doi.org/10.1126/science.aac9439>.
- [20] Y. Qu, et al., Tuning charge transfer process of MoS₂ photoanode for enhanced photoelectrochemical conversion of ammonia in water into gaseous nitrogen, *Chem. Eng. J.* 382 (2020), 123048, <https://doi.org/10.1016/j.cej.2019.123048>.
- [21] C. Backes, et al., Production of highly monolayer enriched dispersions of liquid-exfoliated nanosheets by liquid cascade centrifugation, *ACS Nano* 10 (1) (2016) 1589–1601, <https://doi.org/10.1021/acsnano.5b07228>.
- [22] R.J. Smith, et al., Large-scale exfoliation of inorganic layered compounds in aqueous surfactant solutions, *Adv. Mater.* 23 (34) (2011) 3944–3948, <https://doi.org/10.1002/adma.201102584>.
- [23] V. Nicolosi, et al., Liquid exfoliation of layered materials, *Science* 340 (6139) (2013), 1226419, <https://doi.org/10.1126/science.1226419>.

- [24] J. Mun, et al., Low-temperature growth of layered molybdenum disulphide with controlled clusters, *Sci. Rep.* 6 (1) (2016) 21854, <https://doi.org/10.1038/srep21854>.
- [25] Q. Chen, et al., Atomically flat zigzag edges in monolayer MoS₂ by thermal annealing, *Nano Lett.* 17 (9) (2017) 5502–5507, <https://doi.org/10.1021/acs.nanolett.7b02192>.
- [26] H.R. Gutiérrez, et al., Extraordinary room-temperature photoluminescence in triangular WS₂ monolayers, *Nano Lett.* 13 (8) (2013) 3447–3454, <https://doi.org/10.1021/nl3026357>.
- [27] J. Zhou, et al., Scalable synthesis of high-quality transition metal dichalcogenide nanosheets and their application as sodium-ion battery anodes, *J. Mater. Chem. A* 4 (44) (2016) 17370–17380, <https://doi.org/10.1039/C6TA07425A>.
- [28] J.S. Cho, J.-S. Park, Y.C. Kang, Preparation of hollow Fe₂O₃ nanorods and nanospheres by nanoscale kirkendall diffusion, and their electrochemical properties for use in lithium-ion batteries, *Sci. Rep.* 6 (1) (2016) 38933, <https://doi.org/10.1038/srep38933>.
- [29] F. Li, et al., Few-layered Ti₃C₂T_x MXenes coupled with Fe₂O₃ nanorod arrays grown on carbon cloth as anodes for flexible asymmetric supercapacitors, *J. Mater. Chem. A* 7 (39) (2019) 22631–22641, <https://doi.org/10.1039/C9TA08144E>.
- [30] C. Wang, et al., Conformally coupling CoAl-layered double hydroxides on fluorine-doped hematite: surface and bulk co-modification for enhanced photoelectrochemical water oxidation, *ACS Appl. Mater. Interfaces* 11 (33) (2019) 29799–29806, <https://doi.org/10.1021/acsami.9b07417>.
- [31] Z. Qin, et al., Effect of layer number on recovery rate of WS₂ nanosheets for ammonia detection at room temperature, *Appl. Surf. Sci.* 414 (2017) 244–250, <https://doi.org/10.1016/j.apsusc.2017.04.063>.
- [32] J. Zhang, et al., Monoclinic WO₃ nanomultilayers with preferentially exposed (002) facets for photoelectrochemical water splitting, *Nano Energy* 11 (2015) 189–195, <https://doi.org/10.1016/j.nanoen.2014.10.021>.
- [33] P. Kumar, H. No-Lee, R. Kumar, Synthesis of phase pure iron oxide polymorphs thin films and their enhanced magnetic properties, *J. Mater. Sci.: Mater. Electron.* 25 (10) (2014) 4553–4561, <https://doi.org/10.1007/s10854-014-2203-9>.
- [34] H. Zeng, et al., Optical signature of symmetry variations and spin-valley coupling in atomically thin tungsten dichalcogenides, *Sci. Rep.* 3 (1) (2013) 1608, <https://doi.org/10.1038/srep01608>.
- [35] T.P. Nguyen, et al., Size-dependent properties of two-dimensional MoS₂ and WS₂, *J. Phys. Chem. C* 120 (18) (2016) 10078–10085, <https://doi.org/10.1021/acs.jpcc.6b01838>.
- [36] Y. Wang, et al., Strain-induced direct–indirect bandgap transition and phonon modulation in monolayer WS₂, *Nano Res.* 8 (8) (2015) 2562–2572, <https://doi.org/10.1007/s12274-015-0762-6>.
- [37] J. Tauc, A. Menth, States in the gap, *J. Non-Cryst. Solids* 8–10 (1972) 569–585, [https://doi.org/10.1016/0022-3093\(72\)90194-9](https://doi.org/10.1016/0022-3093(72)90194-9).
- [38] H. Zhang, et al., Gradient tantalum-doped hematite homojunction photoanode improves both photocurrents and turn-on voltage for solar water splitting, *Nat. Commun.* 11 (1) (2020) 4622, <https://doi.org/10.1038/s41467-020-18484-8>.
- [39] Y. Guo, et al., Ni-doped α -Fe₂O₃ as electron transporting material for planar heterojunction perovskite solar cells with improved efficiency, reduced hysteresis and ultraviolet stability, *Nano Energy* 38 (2017) 193–200, <https://doi.org/10.1016/j.nanoen.2017.05.026>.
- [40] Y. Momose, T. Sakurai, K. Nakayama, Thermal analysis of photoelectron emission (PE) and X-ray photoelectron spectroscopy (XPS) data for iron surfaces scratched in air, water, and liquid organics, *Appl. Sci.* 10 (6) (2020), <https://doi.org/10.3390/app10062111>.
- [41] H. Chai, et al., In₂S₃/F-Fe₂O₃ type-II heterojunction bonded by interfacial S-O for enhanced charge separation and transport in photoelectrochemical water oxidation, *Appl. Catal. B: Environ.* 305 (2022), 121011, <https://doi.org/10.1016/j.apcatb.2021.121011>.
- [42] K.M. McCreary, et al., Synthesis of large-area WS₂ monolayers with exceptional photoluminescence, *Sci. Rep.* 6 (1) (2016) 19159, <https://doi.org/10.1038/srep19159>.
- [43] S. Zhang, et al., Layered WS₂/WO₃ Z-scheme photocatalyst constructed via an in situ sulfurization of hydrous WO₃ nanoplates for efficient H₂ generation, *Appl. Surf. Sci.* 529 (2020), 147013, <https://doi.org/10.1016/j.apsusc.2020.147013>.
- [44] M. Guo, et al., WS₂ quantum dots/MoS₂@WO₃-x core-shell hierarchical dual Z-scheme tandem heterojunctions with wide-spectrum response and enhanced photocatalytic performance, *Appl. Catal. B: Environ.* 257 (2019), 117913, <https://doi.org/10.1016/j.apcatb.2019.117913>.
- [45] Q. Wang, et al., Ultrathin two-dimensional BiOBr_xI_{1-x} solid solution with rich oxygen vacancies for enhanced visible-light-driven photoactivity in environmental remediation, *Appl. Catal. B: Environ.* 236 (2018) 222–232, <https://doi.org/10.1016/j.apcatb.2018.05.029>.
- [46] S. Fu, et al., A novel OD/2D WS₂/BiOBr heterostructure with rich oxygen vacancies for enhanced broad-spectrum photocatalytic performance, *J. Colloid Interface Sci.* 569 (2020) 150–163, <https://doi.org/10.1016/j.jcis.2020.02.077>.
- [47] M. Allieta, et al., Electron small polaron and magnetic interactions direct anisotropic growth of silicon-doped hematite nanocrystals, *Cryst. Growth Des.* 20 (7) (2020) 4719–4730, <https://doi.org/10.1021/acs.cgd.0c00496>.
- [48] R. Ciuraru, et al., Heterogeneous reactivity of chlorine atoms with ammonium sulfate and ammonium nitrate particles, *Phys. Chem. Chem. Phys.* 14 (13) (2012) 4527–4537, <https://doi.org/10.1039/C2CP23455F>.
- [49] B.M. Hunter, et al., Effect of interlayer anions on [NiFe]-LDH nanosheet water oxidation activity, *Energy Environ. Sci.* 9 (5) (2016) 1734–1743, <https://doi.org/10.1039/C6EE00377J>.
- [50] W. Xu, W. Tian, L. Li, Two-dimensional nanostructured metal oxide/sulfide-based photoanode for photoelectrochemical water splitting, *Sol. RRL* 5 (6) (2021), 2000412, <https://doi.org/10.1002/solr.202000412>.
- [51] C. Li, et al., Surface, bulk, and interface: rational design of hematite architecture toward efficient photo-electrochemical water splitting, *Adv. Mater.* 30 (30) (2018), 1707502, <https://doi.org/10.1002/adma.201707502>.
- [52] J.-P. Zou, et al., Fabrication of novel heterostructured few layered WS₂-Bi₂WO₆/Bi₃84W_{0.16}O_{6.24} composites with enhanced photocatalytic performance, *Appl. Catal. B: Environ.* 179 (2015) 220–228, <https://doi.org/10.1016/j.apcatb.2015.05.031>.
- [53] K. Jeong, et al., ZnO-TiO₂ core-shell nanowires: a sustainable photoanode for enhanced photoelectrochemical water splitting, *ACS Sustain. Chem. Eng.* 6 (5) (2018) 6518–6526, <https://doi.org/10.1021/acsschemeng.8b00324>.
- [54] Z. Masoumi, M. Tayebi, B.-K. Lee, The role of doping molybdenum (Mo) and back-front side illumination in enhancing the charge separation of α -Fe₂O₃ nanorod photoanode for solar water splitting, *Sol. Energy* 205 (2020) 126–134, <https://doi.org/10.1016/j.solener.2020.05.044>.
- [55] R. Chong, et al., Anion engineering of exfoliated CoAl layered double hydroxides on hematite photoanode toward highly efficient photoelectrochemical water splitting, *Chem. Eng. J.* 366 (2019) 523–530, <https://doi.org/10.1016/j.cej.2019.02.127>.
- [56] M. Kolaei, et al., Decoration of CdS nanoparticles on dense and multi-edge sodium titanate nanorods to form a highly efficient and stable photoanode with great enhancement in PEC performance, *Environ. Sci.: Nano* 8 (6) (2021) 1667–1679, <https://doi.org/10.1039/D1EN00221J>.
- [57] X. Qi, et al., High-performance n-Si/ α -Fe₂O₃ core/shell nanowire array photoanode towards photoelectrochemical water splitting, *Nanoscale* 6 (6) (2014) 3182–3189, <https://doi.org/10.1039/C3NR05429B>.
- [58] M. Tayebi, A. Tayyebi, B.-K. Lee, Photocharged molybdenum-doped BiVO₄ photoanodes for simultaneous enhancements in charge transport and surface passivation, *Sol. Energy* 191 (2019) 427–434, <https://doi.org/10.1016/j.solener.2019.09.004>.
- [59] Y. Fu, et al., A ternary nanostructured α -Fe₂O₃/Au/TiO₂ photoanode with reconstructed interfaces for efficient photoelectrocatalytic water splitting, *Appl. Catal. B: Environ.* 260 (2020), 118206, <https://doi.org/10.1016/j.apcatb.2019.118206>.
- [60] K.-H. Ye, et al., Enhancing photoelectrochemical water splitting by combining work function tuning and heterojunction engineering, *Nat. Commun.* 10 (1) (2019), <https://doi.org/10.1038/s41467-019-11586-y> (3687–3687).
- [61] H. Chai, et al., Surface reconstruction of cobalt species on amorphous cobalt silicate-coated fluorine-doped hematite for efficient photoelectrochemical water oxidation, *ACS Appl. Mater. Interfaces* 13 (40) (2021) 47572–47580, <https://doi.org/10.1021/acsami.1c12597>.
- [62] Z. Masoumi, M. Tayebi, B.-K. Lee, Ultrasonication-assisted liquid-phase exfoliation enhances photoelectrochemical performance in α -Fe₂O₃/MoS₂ photoanode, *Ultrason. Sonochem.* 72 (2021), 105403, <https://doi.org/10.1016/j.ultrasonch.2020.105403>.
- [63] A. Ter Heijne, et al., Identifying charge and mass transfer resistances of an oxygen reducing biocathode, *Energy Environ. Sci.* 4 (12) (2011) 5035–5043, <https://doi.org/10.1039/C1EE02131A>.
- [64] J. Sun, et al., Dual-mode aptasensor assembled by a WO₃/Fe₂O₃ heterojunction for paper-based colorimetric prediction/photoelectrochemical multicomponent analysis, *ACS Appl. Mater. Interfaces* 13 (3) (2021) 3645–3652, <https://doi.org/10.1021/acsami.0c19853>.
- [65] Z. Masoumi, et al., Unified surface modification by double heterojunction of MoS₂ nanosheets and BiVO₄ nanoparticles to enhance the photoelectrochemical water splitting of hematite photoanode, *J. Alloy. Compd.* 890 (2022), 161802, <https://doi.org/10.1016/j.jallcom.2021.161802>.
- [66] R. Wang, et al., Improvement of the water oxidation performance of Ti, F co-modified hematite by surface modification with a Co(salen) molecular cocatalyst, *J. Mater. Chem. A* 8 (41) (2020) 21613–21622, <https://doi.org/10.1039/D0TA07119F>.
- [67] P.S. Bassi, et al., Crystalline Fe₂O₃/Fe₂TiO₅ heterojunction nanorods with efficient charge separation and hole injection as photoanode for solar water oxidation, *Nano Energy* 22 (2016) 310–318, <https://doi.org/10.1016/j.nanoen.2016.02.013>.
- [68] K. Zhang, et al., Sacrificial interlayer for promoting charge transport in hematite photoanode, *ACS Appl. Mater. Interfaces* 9 (49) (2017) 42723–42733, <https://doi.org/10.1021/acsami.7b13163>.
- [69] M. Tayebi, et al., The effect of silver doping on photoelectrochemical (PEC) properties of bismuth vanadate for hydrogen production, *Sol. Energy Mater. Sol. Cells* 200 (2019), 109943, <https://doi.org/10.1016/j.solmat.2019.109943>.
- [70] Y. Hu, et al., Rational design of electrocatalysts for simultaneously promoting bulk charge separation and surface charge transfer in solar water splitting photoelectrodes, *J. Mater. Chem. A* 6 (6) (2018) 2568–2576, <https://doi.org/10.1039/C7TA10361A>.